1 **TITLE**

2 The chemotherapeutic CX-5461 primarily targets TOP2B and exhibits selective activity in high-

3 risk neuroblastoma.

4

5 **AUTHORS**

6 Min Pan[1], William C. Wright[1], Rich Chapple[1], Asif Zubair[1], Manbir Sandhu[2], Jake Batchelder[2, 3],

7 Jonathan Low[3], Kaley B Blankenship[4, 5], Yingzhe Wang[6], Brittney Gordon[5], Payton Archer[4,5],

8 Samuel W. Brady[1], Sivaraman Natarajan[1], Matthew J. Posgai[7], John Schuetz[8], Darcie Miller[2],

9 Ravi Kalathur[2], Siquan Chen[9], Jon Patrick Connelly[10], M. Madan Babu[2], Michael A. Dyer[5, 11],

10 Shondra M. Pruett-Miller[10], Burgess B. Freeman III[6], Taosheng Chen[3], Lucy A. Godley[7], Scott

11 Blanchard[2, 3], Elizabeth Stewart[4, 5], John Easton[1, #], Paul Geeleher[1, #].

12 [1] Department of Computational Biology, St. Jude Children's Research Hospital, Memphis, TN

13 38105, USA

14 [2] Department of Structural Biology, St. Jude Children's Research Hospital, Memphis, TN 38105,

15 USA

16 [3] Department of Chemical Biology and Therapeutics, St. Jude Children's Research Hospital,

17 Memphis, TN 38105, USA

18 [4] Department of Oncology, St. Jude Children's Research Hospital, Memphis, TN 38105, USA

19 [5] Department of Developmental Neurobiology, St. Jude Children's Research Hospital, Memphis,

20 TN 38105, USA

21 [6] Preclinical Pharmacokinetic Shared Resource, St. Jude Children's Research Hospital,

22 Memphis, TN 38105, USA

23   [7] Departments of Medicine and Human Genetics, The University of Chicago, Chicago, IL 60637,

24   USA

25   [8] Department of Pharmaceutical Sciences, St. Jude Children's Research Hospital, Memphis, TN

26   38105, USA

27   [9] Cellular Screening Center, The University of Chicago, Chicago, IL 60637, USA

28   [10] Department of Cell and Molecular Biology, St. Jude Children's Research Hospital, Memphis,

29   TN 38105, USA

30   [11] Howard Hughes Medical Institute, Chevy Chase, MD 20815, USA

31   [#] Correspondence: paul.geeleher@stjude.org (P.G.); john.easton@stjude.org (J.E.)

32

33   **ABSTRACT** (approx. 150 words)

34   Survival in high-risk pediatric neuroblastoma has remained around 50% for the last 20 years,

35   with immunotherapies and targeted therapies having had minimal impact. Here, we identify the

36   small molecule CX-5461 as selectively cytotoxic to high-risk neuroblastoma and synergistic with

37   low picomolar concentrations of topoisomerase I inhibitors improving survival *in vivo* in

38   orthotopic patient-derived xenograft neuroblastoma mouse models. CX-5461 recently

39   progressed through phase I clinical trial as a first-in-human inhibitor of RNA-POL I. However, we

40   also use a comprehensive panel of *in vitro* and *in vivo* assays to demonstrate that CX-5461 has

41   been mischaracterized and that its primary target at pharmacologically relevant concentrations,

42   is in fact topoisomerase II beta (*TOP2B*), not RNA-POL I. These findings are important because

43   existing clinically approved chemotherapeutics have well-documented off-target interactions

44   with TOP2B, which have previously been shown to cause both therapy-induced leukemia and

45   cardiotoxicity—often-fatal adverse events, which can emerge several years after treatment.

46   Thus, while we show that combination therapies involving CX-5461 have promising anti-tumor

47   activity *in vivo* in neuroblastoma, our identification of TOP2B as the primary target of CX-5461

48   indicates unexpected safety concerns that should be examined in ongoing phase II clinical trials

49   in adult patients before pursuing clinical studies in children.

50

INTRODUCTION

Neuroblastoma is a pediatric cancer of the developing peripheral nervous system and the most common solid tumor in children[1]. Pediatric cancers have different mutation profiles compared to adult cancers, typically exhibiting far fewer targetable oncogene mutations[2]. Additionally, the low mutation burden and resulting lack of neoantigens means immunotherapies have had an only modest impact[3]. Consequently, the overall survival in high-risk neuroblastoma has remained around 50% for the past 20 years[4], meaning a promising small molecule inhibitor is of tremendous interest to treat this devastating disease.

Since the release of the Cancer Cell Line Encyclopedia (CCLE)[5] and the Genomics of Drug Sensitivity in Cancer (GDSC)[6], large drug screening datasets in cancer cell lines have emerged as a valuable resource for identifying new therapeutic strategies to treat pediatric cancers, facilitating discoveries that could not have been made based on mutation profiles alone. For example, these datasets provided the original evidence that PARP inhibitors would be effective treating Ewing's Sarcoma, which has since proven to have clinical activity in combination with DNA damaging agents[7,8]. Perturbational screens in these cell lines have also motivated the development of EZH2 inhibitors in pediatric rhabdoid tumors[9] and BRD4 inhibitors in neuroblastoma[10,11]. However, the rapid growth of these datasets[12–14] means systematic interrogation of the pediatric data has not been carried out, limiting the potential for prioritizing promising targets in these diseases.

Here, we mined these datasets to identify an unexpected, reproducible, selective effect of the compound CX-5461 in high-risk pediatric neuroblastoma. CX-5461 recently progressed through phase I clinical trial as a first-in-human selective inhibitor of RNA-POL I[15], but has also been reported to target DNA G-quadruplex structures in vitro[16,17] and (by a single study) TOP2A[18]. Motivated by the striking drug screening results, we performed a comprehensive study in orthotopic patient-derived xenograft (PDX) bearing mice to show that CX-5461 has anti-

4

76   neuroblastoma activity *in vivo* at pharmacologically relevant dosages derived using an *in vivo*

77   pharmacokinetics modeling approach. However, we also show that CX-5461 is

78   mischaracterized and its primary target at physiological concentrations is in fact TOP2B, which

79   because of this gene's unique functional role, completely changes the clinical trajectory of this

80   compound in terms of patient stratification, drug combinations, and likely side-effect profiles.

81   Critically, *TOP2B* is highly expressed in some normal cells and off-target drug interactions with

82   this gene have previously been implicated in late-emerging therapy-induced acute

83   leukemias[19,20] and cardiotoxicity[21], which often lead to death. Thus, while CX-5461 has

84   promising anti-tumor activity *in vivo*, our results indicate that it also has the potential to cause

85   previously unanticipated patient harm, which should be investigated in adults before clinical

86   studies are proposed in children.

87

88 **RESULTS**

89 **CX-5461 exhibits selective and potent activity against neuroblastoma cell lines.**

90 We first devised a quantitative metric to identify compounds with selective activity against

91 neuroblastoma cell lines in large drug screening datasets (similar to Durbin *et al.*[10]). For each

92 drug, we ranked cell lines by their IC_{50}, identified the rank of the median neuroblastoma cell line,

93 then normalized this value to a 0-1 scale by dividing by the total number of cell lines screened

94 against this drug—we refer to this as a "Selectivity Score". We calculated Selectivity Scores for

95 each drug in the most recent release of the Sanger Institute's GDSC cell line drug screening

96 dataset, where a total of 265 drugs were screened against 1,001 cancer cell lines[22], including 31

97 neuroblastoma cell lines, the most of currently available datasets. Drugs with the highest

98 Selectivity Score included several already in investigation in neuroblastoma (Fig. 1A; Table S1),

99 for example, ranked #3 and #4 were IGF1R inhibitors (linsitinib and BMS-754807)[23].

100 Surprisingly, the second most selective drug for neuroblastoma was CX-5461, a compound that

101 recently completed phase I clinical trial as a first-in-human selective inhibitor of RNA-POL I, but

102 is not currently in clinical investigation in neuroblastoma[4]. The selective activity was striking (Fig.

103 1B, Fig. S1A, $P = 5.2 \times 10^{-6}$ from t-test of neuroblastoma IC_{50} values vs all other cell lines) with

104 almost half of neuroblastoma cell lines achieving an IC_{50} in the nanomolar range. We obtained

105 and rescreened 8 of the GDSC cell lines with CX-5461 and achieved highly consistent results

106 (Fig. 1C, $r = 0.94$, $P = 5.7 \times 10^{-4}$; Fig. S1B-C). Additionally, CX-5461 was included in PRISM, a

107 recent independent study[12] that screened 4,518 drugs against 578 cancer cell lines using a new

108 high-throughput multiplex sequencing-based assay. Although only 10 neuroblastoma cell lines

109 were included, neuroblastoma remained the second most sensitive group to CX-5461 among

110 the 24 cancer types screened (Fig. 1D). The overall trend for Selectivity Scores was also

111 recapitulated in PRISM (Fig. 1E; Fig. S1D), with CX-5461 remaining among the most selective

112 drugs for neuroblastoma cell lines.

113 To deduce whether CX-5461 may favor specific subclasses of neuroblastoma, we next sought

114 to identify genetic predictors of CX-5461 response in these neuroblastoma cell lines. Using the

115 GDSC's exome sequencing data we identified *MYCN* amplification and *TP53* mutation as

116 independently predictive of response ($P = 6.4 \times 10^{-4}$ from a multivariate linear model; $R^2 = 0.4$).

117 The effect sizes were large; *TP53* mutation was associated with a 17.45 ± 4.7 (mean effect +/-

118 95% CI) fold increase in IC_{50}, while *MYCN* amplification was associated with a 10.9 ± 5.6-fold

119 decrease in IC_{50}. We tested these predictions *in vitro* using short hairpin RNA (shRNA)

120 knockdown of *MYCN* ($P < 0.05$ for each of 3 independent shRNAs, Fig. 1G-H) and CRISPR

121 knockout of *TP53* ($P = 2.3 \times 10^{-3}$, Fig. 1I) in CHP-134 (*MYCN* amp, *TP53* wt.) neuroblastoma

122 cells, identifying a causal relationship with CX-5461 IC_{50} in both cases. We recalculated the

123 Selectivity Scores for only *MYCN* amplified *TP53* wild-type neuroblastoma cell lines—

124 representative of high-risk disease—where CX-5461 was the #1 most selective compound for

125 these cell lines (Fig. S1E & S1F). Thus, CX-5461 is of particular interest in the high-risk

126 subgroup of neuroblastoma, where *MYCN* amplification is the primary driver and patient

127 outcomes are extremely poor.

128

129 **CX-5461 kills neuroblastoma cells at low concentrations that do not inhibit RNA-POL I.**

130 CX-5461 recently completed phase I clinical trial as a selective inhibitor of RNA-POL I[24]. To

131 confirm that this was indeed the mechanism-of-action against neuroblastoma cells, we

132 performed a standard assay to determine whether CX-5461 interferes with RNA-POL I

133 activity[25]—using qPCR to the short-lived internal transcribed spacer (ITS) region of the 45S

134 rRNA transcript. We applied this in CX-5461-treated CHP-134 and IMR-5 (both highly CX-5461

135 sensitive) neuroblastoma cell lines. Surprisingly, we observed no inhibition of RNA-POL I

136 activity in these cell lines at the low sub-micromolar concentrations at which CX-5461 was

137 effective (Fig. 1J, S1G-H). However, in four CX-5461-resistant neuroblastoma cell lines, where

138   higher CX-5461 concentrations could be tolerated, we observed inhibition of RNA-POL I (Fig.

139   1J). This is consistent with RNA-POL I inhibition emerging either as an off-target effect or as a

140   consequence of inhibiting the primary drug target. We validated these observations using a 5-

141   ethynyl uridine (EU) incorporation assay, where again there was no inhibition of RNA synthesis

142   at the low concentrations of CX-5461 that were effective against CHP-134 and IMR-5 cells (Fig.

143   1K). The resistant cell line KELLY, which could be treated with higher concentrations of CX-

144   5461, again showed clear inhibition of RNA-POL I. We also identified no significant associations

145   between the baseline expression levels of RNA-POL I complex genes and CX-5461 IC$_{50}$ in

146   GDSC neuroblastoma cell lines (Fig. 1L) or between the median expression of RNA-POL I

147   complex genes and response to CX-5461 (Fig. 1M). Finally, treatment with CX-5461 for 48 or

148   72 hours did not decrease the levels of mature cellular rRNA in neuroblastoma cells (Fig. S1I-J).

149   These results indicate that CX-5461's anti-cancer activity may not exclusively result from

150   selective inhibition of RNA-POL I. Instead, these findings suggest that CX-5461 may be active

151   against neuroblastoma cell lines by one or more additional mechanisms independent of impacts
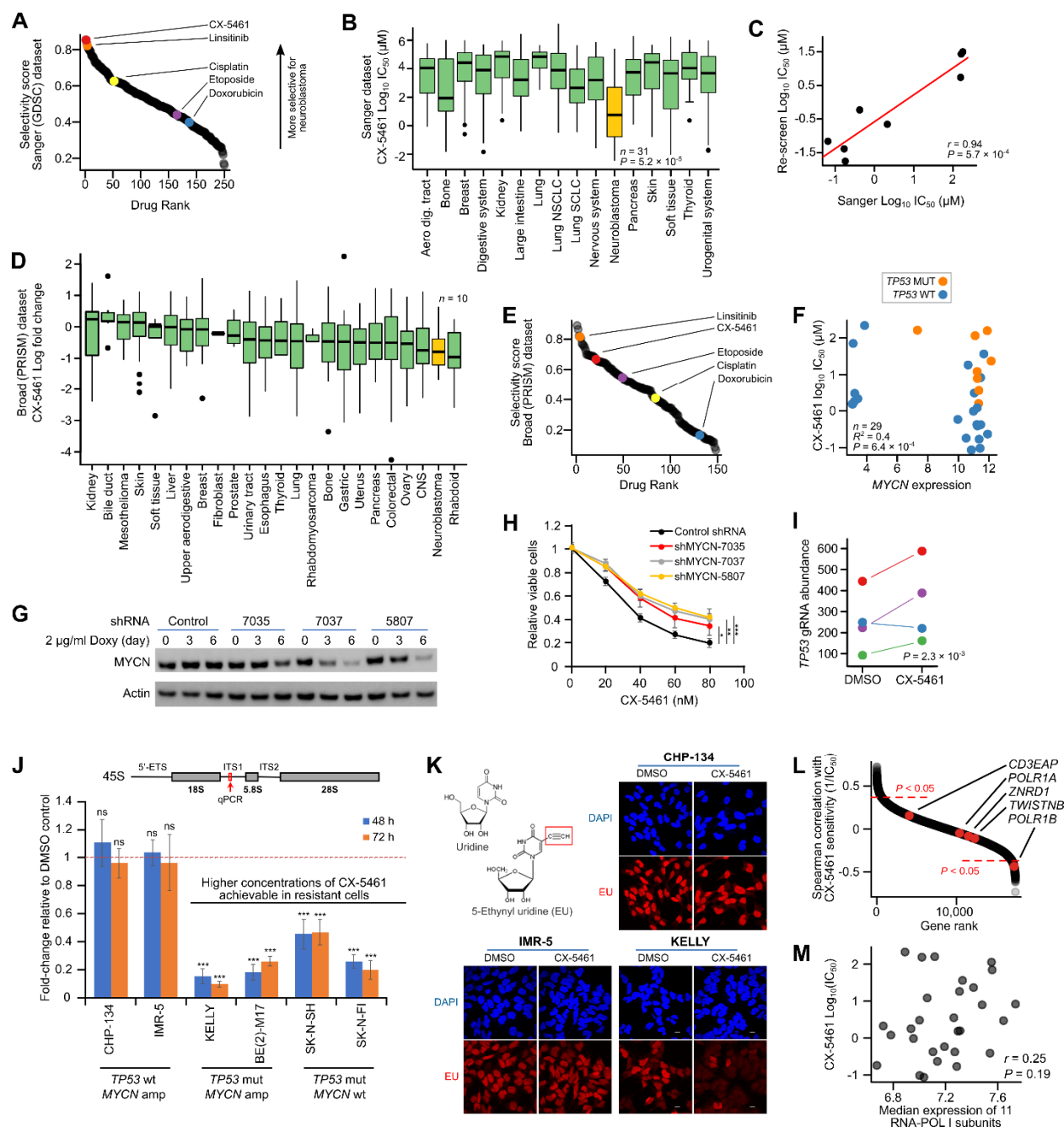
152   on rRNA synthesis.

153

Figure 1. Neuroblastoma cell lines are selectively sensitive to CX-5461.

A. Waterfall plot showing summary score representing selectivity for neuroblastoma cell lines plotted for each of 265 drugs screened by GDSC, where the y-axis is the observed scores, and the x-axis is the drug rank. A higher value on the y-axis implies greater selective activity of the drug against neuroblastoma cell lines. CX-5461 is highlighted in red.

B. Boxplot of $\log_{10}(IC_{50})$ values for CX-5461 for all non-hematological cancer cell lines screened by GDSC (see Fig. S1A).

C. Scatterplot of $\log_{10}(IC_{50})$ values for CX-5461 for 8 cell lines screened by GDSC (x-axis) and re-screened in this study (y-axis).

9

163   D. Boxplot of $\log_{10}$(fold change) values for CX-5461 for all cell lines screened by PRISM. Fold-changes
164   represent the difference in cell viability of drug treated vs. control cells in the PRISM assay, estimated by
165   sequencing each cells unique barcode. A lower fold-change implies higher drug effectiveness. Note: there
166   were no rhabdoid cell lines in the GDSC discovery dataset.
167   E. Waterfall plot showing summary score representing selectivity for neuroblastoma cell lines plotted for each
168   of 148 drugs screened in PRISM (shown for drugs screened by both PRISM and GDSC), where the y-axis
169   are the observed scores, and the x-axis is the drug rank.
170   F. Scatterplot showing *MYCN* expression level (x-axis) against $\log_{10}(IC_{50})$ values for CX-5461 in GDSC (y-
171   axis). The points are colored by *TP53* mutation status.
172   G. Western blot showing MYCN protein levels following *MYCN* knockdown using 3 independent shRNAs in
173   CHP-134 cells. β-Actin was used as loading control. Doxy, doxycycline.
174   H. Viability of CHP-134 cells following *MYCN* knockdown under treatment with CX-5461. Cells were
175   transduced with one of three independent *MYCN* shRNAs or a negative control shRNA. After 6 days of
176   incubation in medium with 2 µg/ml doxycycline, cells were treated with CX-5461 for 3 days. Cell viability
177   was measured with MTS. Data represent mean ± SD of 3 independent experiments. *$P < 0.05$, **$P < 0.01$,
178   ***$P < 0.001$.
179   I. Stripchart showing the relative abundance of 4 independent *TP53* guide RNAs in a genome-wide CRISPR
180   screen (y-axis) in either a DMSO or CX-5461 treated CHP-134 neuroblastoma cell line.
181   J. Pre-rRNA 45S expression (y-axis) in CX-5461 treated cell lines relative to DMSO, determined by RT-
182   qPCR with primers located in an internal transcribed spacer (ITS) region of the rRNA transcript. Data
183   represent mean ± SD of 3 independent experiments. ***$P < 0.001$; ns, no significant difference to DMSO
184   control. CX-5461 concentration: CHP-134, 0.2 µM; IMR-5, 0.05 µM; KELLY, 2 µM; BE(2)-M17, 10 µM;
185   SK-NSH, 2 µM; SK-N-FI, 20 µM.
186   K. EU incorporation assay to assess global nascent RNA transcription. CHP-134, IMR-5 and KELLY cells
187   were treated with CX-5461 for 24 h. 1 mM EU was added at 30 min (CHP-134, IMR-5) or 1 h (KELLY)
188   before cell fixation. Nascent RNA was labeled with EU (red). Cell nuclei were stained with DAPI (blue).
189   CX-5461 concentration: CHP-134, 0.2 µM; IMR-5 0.05 µM; KELLY, 2 µM. Scale bar = 10 µm.
190   L. Waterfall plot showing Spearman's correlation of the expression of all genes in GDSC with the reciprocal
191   of CX-5461 IC_{50} (y-axis) in 29 neuroblastoma cell lines. Higher values on the y-axis imply that high
192   expression of a gene is associated with greater sensitivity to CX-5461. Genes unique to the RNA-POL I
193   complex (those not shared with RNA-POL II) are highlighted in red.
194   M. Scatterplot showing the correlation of the median expression level of 11 genes of the RNA-POL I complex
195   (x-axis) for which a gene expression estimate was available in GDSC with CX-5461 $\log_{10}(IC_{50})$ (y-axis) in
196   29 neuroblastoma cell lines.

197

CX-5461's is a topoisomerase II inhibitor.

199   The genome-wide CRISPR knockout screen has emerged as a powerful, unbiased assay for

200   determining the mechanism-of-action of small molecules[26]. The workflow involves culturing cells

201   stably expressing Cas9 with or without the drug of interest, performing genome-wide CRISPR

202   gene knockout, and comparing the relative abundance of different guide RNAs in drug-treated

203   vs control cells; this acts as a proxy for the proportion of surviving cells that have undergone

204   each gene knockout (Fig. 2A). We performed such a screen in CHP-134 neuroblastoma cells

205   treated with 0.04 µM CX-5461 or DMSO control, allowing us to identify genes required for

206   growth of CHP-134 cells in the presence of CX-5461. Notably, none of the top hits had any

207   obvious relationship to RNA-POL I or DNA G-quadruplexes, however, there was a clear

208   enrichment of genes related to DNA-damage response (Fig. 2B, Fig. S2A-B). Remarkably, all

209   three of the most significant knockouts had a direct relationship to topoisomerase II (Fig. 2C-E):

210   TDP2 catalyzes the removal of the covalent bonds between topoisomerase II and DNA[27], LIG4

211   is a DNA ligase that rejoins double-strand breaks caused during normal topoisomerase II

212   activity[28], and inhibition of FZR1 has previously been shown to sensitize cells to topoisomerase

213   II inhibitors[29]. We queried a recently published resource[26] that performed CRISPR knockout

214   screens in human retinal epithelial cells treated with 31 DNA damaging agents and confirmed

215   that *TDP2*, *LIG4*, and *FZR1* knockouts all sensitize these cells to the known topoisomerase II

216   inhibitors doxorubicin and etoposide (Fig. 2F-G). These results suggest that CX-5461's primary

217   target at pharmacologically relevant concentrations is in fact topoisomerase II. This is especially

218   plausible given that CX-5461 is a fluoroquinolone derivative[30] and maintains structural similarity

219   to these antibiotics, which target bacterial DNA gyrase—an ortholog of human topoisomerase

220   II[31].

221   To investigate further whether CX-5461's structure is consistent with that of a topoisomerase II

222   inhibitor, we performed molecular dynamics simulations, using existing TOP2A and TOP2B

223   protein structures. The *in silico* binding of CX-5461 was consistent with that of a classical

224   topoisomerase II poison: This is the most common mechanism for topoisomerase II inhibitors

225   (including fluoroquinolones, etoposide, and doxorubicin), where the drug traps the

226   topoisomerase protein covalently bound to DNA, leading to DNA damage and cell death[32]. CX-

227   5461 interacts with the DNA breakpoint, collectively surrounded by the TOP2A/B DNA binding

228   domains (Fig. 2H). We also found that CX-5461 interactions differ between TOP2A and TOP2B,

229   interacting with largely non-analogous amino acids of the respective proteins (Fig. 2I). We

11

230   calculated the relative binding affinity of the CX-5461 ligand to the TOP2A/B proteins and noted

231   a slightly increased affinity of the ligand to TOP2B. (Fig. 2J).

232   We performed several orthogonal assays to test the hypothesis that CX-5461 is a

233   topoisomerase II poison. We first performed a band depletion assay[33], to assess the

234   stabilization of TOP2-DNA covalent complexes (called the TOP2 cleavable complex (TOP2cc)),

235   following CX-5461 treatment. This assay showed a clear depletion of free TOP2A and TOP2B

236   protein, consistent with these proteins being trapped to DNA following treatment with CX-5461

237   (Fig. 2K). The decrease of free TOP2 was dose-dependent and comparable to the positive

238   control TOP2 poison doxorubicin (Fig. 2L). The cisplatin-treated negative control showed no

239   change (Fig. 2M). CX-5461 did not affect TOP1 (Fig. 2K), suggesting its activity is selective to

240   TOP2. We next used a complementary assay, the rapid approach to DNA adduct recovery

241   (RADAR) assay, to further assess the ability of CX-5461 to form TOP2cc[34]. This revealed CX-

242   5461 treatment-induced TOP2cc formation, for both TOP2A and TOP2B, in all four

243   neuroblastoma cell lines tested (Fig. S2C), again consistent with CX-5461 trapping TOP2 to

244   DNA and behaving as a classical topoisomerase II poison.
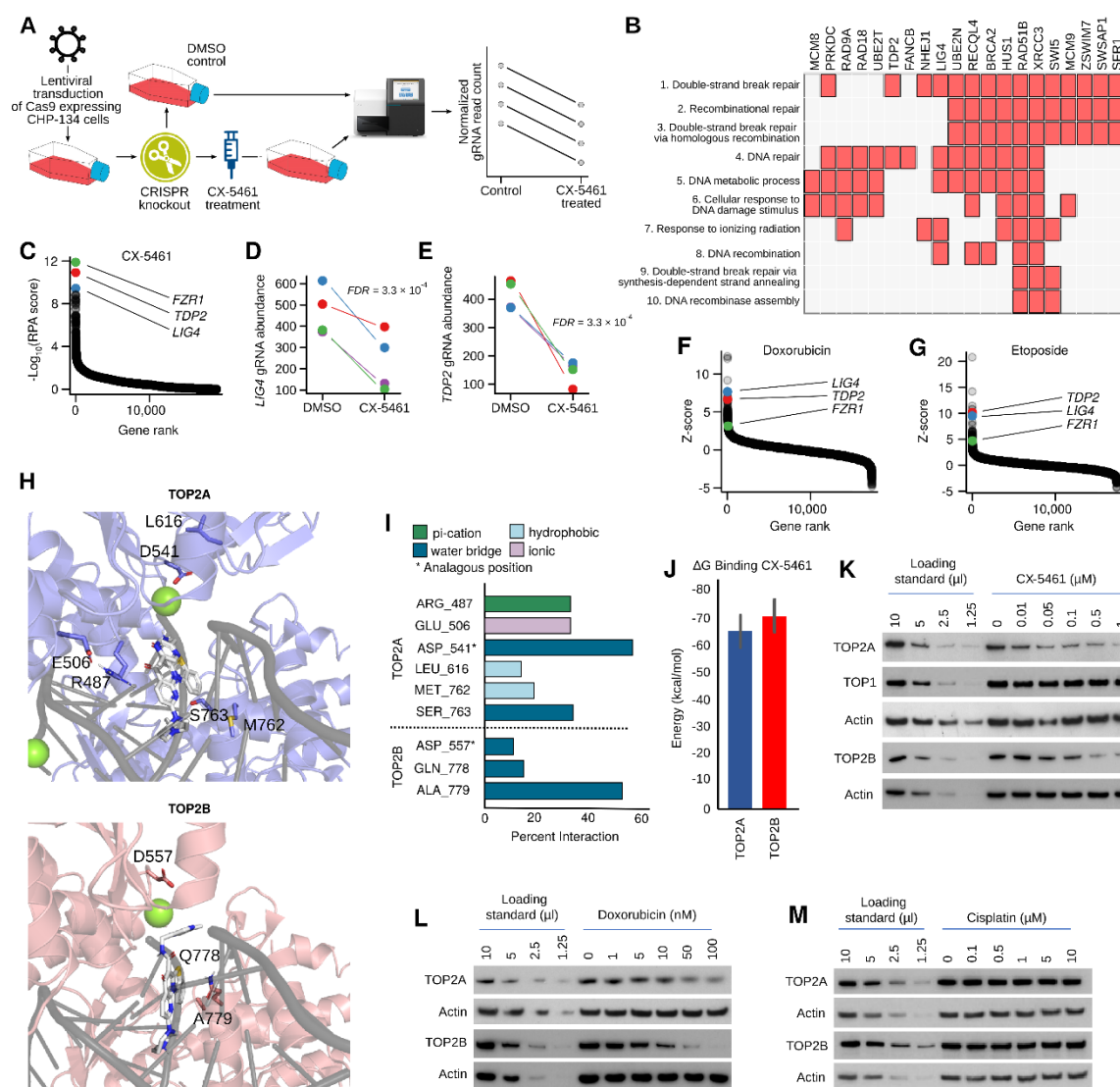
245

Figure 2. CX-5461 is a topoisomerase II inhibitor.

A. Schematic of CRISPR knockout screening strategy. CX-5461 (0.04μM) and DMSO (no treatment negative control) treated CHP-134 cells were subjected to whole-genome CRISPR screen.

B. Clustergram generated by Enrichr showing the assignment of statistically significant (red boxes) gene knockouts to the most highly enriched GO (2018) Biological Processes (y-axis). Genes with an FDR < 0.05 (n = 40) were used as input.

C. Waterfall plot highlighting the top hits in our genome-wide CRISPR knockout screen in CHP-134 cells. Genes are ranked (x-axis) by -log$_{10}$(RPA score) (y-axis).

D. Stripchart showing the relative abundance of 4 independent *LIG4* guide RNAs in our genome-wide CRISPR screen (y-axis) in either DMSO or CX-5461 treated CHP-134 cells.

E. Like (D) but for *TDP2*.

F. Waterfall plot summarizing CRISPR knockout screening data obtained from Oliveri *et al.* for the topoisomerase II inhibitor doxorubicin. Higher values on the y-axes imply that knockout has sensitized cells to doxorubicin. *TDP2, LIG4,* and *FZR1* are highlighted in red, blue and green respectively.

G. Like (F) but results shown for the topoisomerase II inhibitor etoposide.

13

261 H. Representative poses from equilibrated molecular dynamics simulations of CX-5461 bound to TOP2A (top)
262 or TOP2B (bottom). DNA strands are shown in gray. CX-5461 is displayed in white, and its heteroatoms
263 colored blue (nitrogen), red (oxygen), and yellow (sulfur). Green represents magnesium ions.

264 I. Percentage of CX-5461 interactions with TOP2A or TOP2B simulations. Residues interacting with either
265 protein are listed if they conferred $\geq$ 10% interaction with CX-5461. Bar colors correspond to type of
266 interaction. (*) indicates residues in the same position when the two proteins are superimposed.

267 J. Weighted average of the relative binding affinity for CX-5461 is plotted for TOP2A (65.2 kcal/mol) and
268 TOP2B (-70.7 kcal/mol). Error bars represent the standard deviation of the weighted averages ($P = 0.01$ from t-
269 test).

270 K-M. Band-depletion assay for CX-5461 (K), doxorubicin (L), and cisplatin (M) treated CHP-134 cells. Cells
271 were exposed to agents at their approximate IC_{50} for 4 h. Cell lysates were collected for SDS-PAGE. Cell
272 lysates from untreated cells were used as loading standard.

273

274 **Low sub-micromolar concentrations of CX-5461 induce cell cycle arrest and kill**

275 **neuroblastoma cells by causing DNA damage and cell death by apoptosis.**

276 The mechanism of drug-induced cell death by classical topoisomerase II poisons, such as

277 etoposide and doxorubicin is well understood. These drugs trap topoisomerase protein to DNA,

278 and these DNA-topoisomerase complexes are converted to DNA double-strand breaks when

279 encountered by the DNA replication or transcription machinery, leading to cell death by

280 apoptosis[35].

281 To investigate whether this was the mechanism of cell death in neuroblastoma cells susceptible

282 to sub-micromolar concentrations of CX-5461, we first used flow cytometry to quantify

283 neuroblastoma cells staining positive for annexin V and propidium iodide (PI), canonical

284 markers of apoptosis and cell death respectively, following CX-5461 treatment at 0.1 µM, 0.2

285 µM and 0.5 µM over 48h. These assays showed that CX-5461 was causing cell death by

286 apoptosis at these low concentrations in CX-5461 sensitive CHP-134 and IMR-5 neuroblastoma

287 cells (Fig. 3A-3C). Induction of cell death by apoptosis at low concentrations of CX-5461 was

288 confirmed by Western blot for cleaved PARP (c-PARP, Fig. 3D) in CHP-134 and IMR-5 cell

289 lines.

290   We next investigated CX-5461's DNA damaging effects, using immunofluorescence for

291   canonical DNA damage markers γ-H2AX, 53BP1 (Fig. 3E, Fig. S3A), and RPA (Fig. S3B) in

292   CHP-134 and IMR-5 cell lines. Indeed, these markers were evident following treatment with

293   nanomolar concentrations of CX-5461 for 24 hours. We confirmed DNA damage using a single-

294   cell alkali gel electrophoresis (comet) assay in CHP-134 cells treated with 0.2 µM for 30 minutes

295   or 24 hours, with DNA damage evident at 30 minutes and increasing at 24 hours (Fig. 3F, Fig.

296   S3C). Furthermore, using cell cycle analysis and an EdU incorporation assay, we found

297   evidence of S phase cell cycle arrest (Fig. 3G) and deceleration of active DNA synthesis (Fig.

298   3H), started 8 h post CX-5461 treatment. Moreover, γ-H2AX staining was heavily enriched in

299   cells with active DNA synthesis (Fig. 3I). Together, these data suggest that DNA replication

300   stress was induced and DNA damage was generated during DNA replication. Western blot

301   revealed phosphorylation of cell cycle checkpoints CHK1, CHK2, and p53(S15) in CX-5461

302   treated CHP-134 and IMR-5 cells, indicating activation of the DNA-damage response (Fig. S3D-

303   EI). We also found that cells surviving over a 24 h treatment with CX-5461 accumulated in the

304   G2/M phase of cell cycle (Fig. 3G), consistent with arrested cells undergoing DNA repair. In

305   summary, the DNA damaging effects of low sub-nanomolar concentrations of CX-5461 (not

306   sufficient to inhibit RNA-POL I) follow the hallmark DNA-damaging activities of topoisomerase II
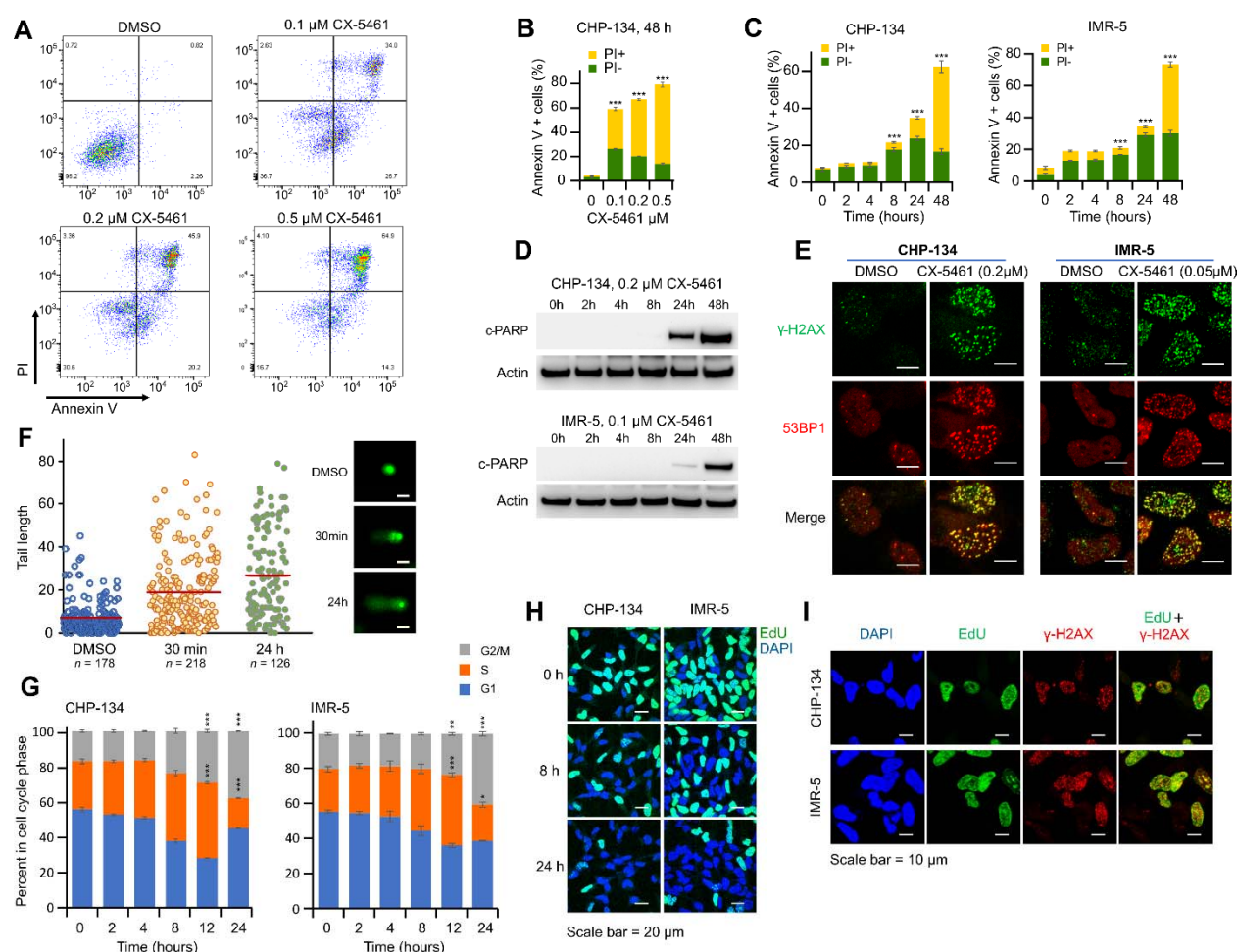
307   poisons.

Figure 3. CX-5461 causes DNA damage and cell death by apoptosis in neuroblastoma cells at low concentrations that do not inhibit RNA POL I.

A. Flow cytometry data showing apoptosis in CHP-134 cells. The cells were treated with CX-5461 for 48 h with indicated concentrations. Induction of cell apoptosis was measured by annexin V (x-axis) and cell death by propidium iodide (PI) staining (y-axis).

B. Quantification of data in Fig. 2E. The y-axis shows the percentage of annexin V positive cells, with the proportion of PI positive cells shown in yellow, for increasing concentrations of CX-5461 (x-axis). Data represent the mean ± SD of 3 independent experiments. ***$P < 0.001$.

C. Quantification of flow cytometry data showing apoptosis up to 48 h in CHP-134 (left panel) and IMR-5 (right panel) cells. CHP-134 cells were treated with 0.2 µM and IMR-5 cells with 0.1 µM of CX-5461. The y-axis shows the percentage of annexin V positive cells, with the proportion of PI positive cells shown in yellow (x-axis). Data represent the mean ± SD of 3 independent experiments. ***$P < 0.001$.

D. Western blots for cleaved PARP (c-PARP). Cells were treated with CX-5461 for the time and concentration indicated. β-Actin was used as a loading control.

E. Co-localization of 53BP1 and γ-H2AX. Cells were treated with DMSO or CX-5461 (0.2 µM for CHP-134 and 0.05 µM for IMR-5) for 24 h, cells were stained with 53BP1 (red) and γ-H2AX (green) antibodies for immunofluorescence. Scale bar = 10 µm.

F. Comet assay in CHP-134 cells. Cells were treated with DMSO or 0.2 µM CX-5461 for 30 min or 24 h (x-axis) before electrophoresis. Tail length (left) and representative images (right) are shown. The red line indicates the mean value of tail length in each group. Scale bar = 5 µm.

16

329   G. Bar graph showing results of cell cycle analysis. CHP-134 and IMR-5 cells were treated with CX-5461
330   (CHP-134, 0.2 µM; IMR-5, 0.05 µM) for the time indicated (x-axis) and stained with PI for flow cytometry
331   analysis. The proportion of cells in each cell cycle phase (y-axis) was determined by DNA content. Data
332   represent the mean ± SD of 3 independent experiments. $*P < 0.05$, $**P < 0.01$, $***P < 0.001$.

333   H. CHP-134 and IMR-5 cells were treated with 0.2 µM CX-5461 and 0.05 µM CX-5461 respectively for the
334   time indicated. 2 hours before cell fixation, 10 µM EdU was added to the medium. Blue, DAPI; green,
335   EdU. Scale bar = 20 µm.

336   I. CX-5461 induced DNA damage (γ-H2AX, red) was enriched in cells with active DNA synthesis (positive
337   for EdU (green) labeling). CHP-134 cells were treated with 20 µM EdU and 0.2 µM CX-5461 for 3 h.
338   IMR-5 cells were treated with 10 µM EdU and 0.1 µM CX-5461 for 3 h. Immunofluorescence was then
339   carried out in these cells. Scale bar = 10 µm.

340

CX-5461 primarily targets the TOP2B paralog.

342 The findings above initially seemed to be consistent with single isolated study, which used a

343 computational systems biology approach to predict TOP2A as CX-5461's primary target[18]. This

344 is exciting as TOP2A is one of the most successful drug targets in cancer[36]; however, TOP2A

345 as CX-5461's primary target leaves critical inconsistencies. Why did other topoisomerase II

346 poisons (etoposide, doxorubicin) not also show selective activity against neuroblastoma cell

347 lines (Fig. 1A & 1E)? Moreover, why has CX-5461 been shown to inhibit RNA-POL I in many

348 different cell types, including non-cycling cells[37], which do not express TOP2A[38]? As was hinted

349 at in our molecular dynamic simulations, the answers stem from CX-5461's interaction with

350 TOP2B—which despite structural similarity is highly functionally distinct from *TOP2A*[19], thus

351 completely altering the clinical trajectory of this compound.

352 We first observed that although *TOP2A* and *TOP2B* were both overexpressed in neuroblastoma

353 cell lines (Figure S4A-B), the magnitude of *TOP2B* overexpression was substantially larger.

354 Whereas the median expression of *TOP2A* was 31.3% higher than the median in all other

355 cancer cell lines in DepMap RNA-seq data ($P = 2 \times 10^{-3}$, Figure 4A), the median expression of

356 *TOP2B* was 87.1% higher ($P = 1.3 \times 10^{-7}$, Figure 4B). Additionally, *TOP2B* expression was

357 among the most highly negatively correlated genes with CX-5461 IC$_{50}$ in GDSC neuroblastoma

358 cell lines ($r = -.58$, $P = 1 \times 10^{-3}$, Fig. 4C), and this was the 2nd highest negative correlation with

17

359   *TOP2B* of all drugs screened (Fig. 4D). Based on these observations, we hypothesized that CX-

360   5461's cytotoxicity may occur through preferential targeting of TOP2B, unlike existing TOP2

361   poisons etoposide and doxorubicin, whose effects primarily result from trapping TOP2A on

362   DNA.

363   To test this hypothesis, we first performed an shRNA knockdown of *TOP2A* and *TOP2B* using

364   five independent shRNAs in CHP-134 cells. Remarkably, although knockdown of *TOP2A*

365   conferred resistance to etoposide, doxorubicin and CX-5461, knockdown of *TOP2B* only caused

366   resistance to CX-5461 (Fig. 4F-G, $P < 0.001$). The cisplatin-treated negative control was not

367   affected by knockdown of either gene (Fig. 4F). We next used CRISPRa to overexpress both

368   *TOP2A* and *TOP2B* in CHP-134 cells and although overexpression of either gene increased

369   sensitivity to CX-5461, doxorubicin, and etoposide, the effect of *TOP2B* overexpression was

370   greater for CX-5461 (Fig. 4H-I), corroborating the idea that CX-5461 has a strong interaction

371   with TOP2B.

372   To confirm direct inhibition of topoisomerase II paralogs by CX-5461, we next performed an *in*

373   *vitro* topoisomerase activity assay, which tests a compound's ability to inhibit the decatenation

374   of purified catenated kinetoplast DNA (kDNA) plasmids in the presence of purified

375   topoisomerase protein (Fig. 4J). CX-5461 inhibited the activity of both TOP2A and TOP2B—

376   strikingly at concentrations substantially lower than etoposide (Fig. 4K). The negative control

377   ciprofloxacin, which targets type II topoisomerase in prokaryotes and is a fluoroquinolone with

378   structural similarity to CX-5461, had no activity in this assay. By comparing the concentration of

379   CX-5461 required to inhibit TOP2A or TOP2B in this highly controlled *in vitro* system, we directly

380   quantified CX-5461's preference for TOP2B (Fig. S4C-E). Remarkably, CX-5461 was between

381   2- and 4-fold more effective at inhibiting TOP2B, compared to TOP2A ($P = 2.8 \times 10^{-4}$, Fig. 4L).

382   Etoposide and doxorubicin had similar activity against both paralogs. We observed similar

383   trends when we also performed a complementary topoisomerase activity assay to determine

18

384   CX-5461's ability to inhibit topoisomerase II-induced relaxation of purified supercoiled DNA,

385   where CX-5461 performed similarly to doxorubicin and etoposide, with a clear preference for

386   TOP2B (Fig. 4M; Fig. S4E). While these multiple orthogonal lines of evidence demonstrate that

387   CX-5461 exhibits classical TOP2 poison activity, our findings are indicative that the primary CX-
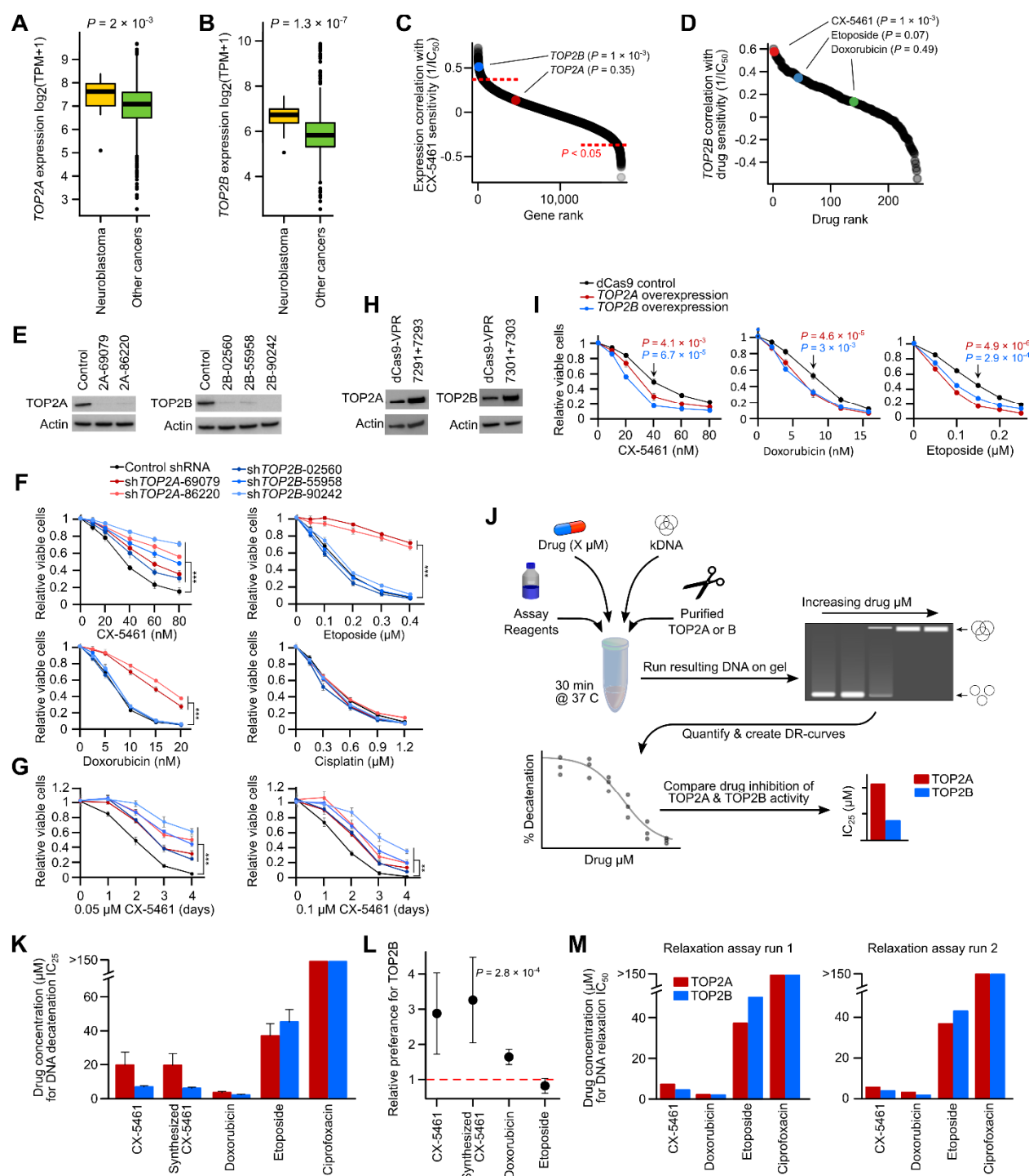
388   5461 target is TOP2B.

389

Figure 4. CX-5461 primarily targets the TOP2B paralog.

A. Boxplot showing the $\log_2$(TPM+1) expression of *TOP2A* (y-axis) in DepMap neuroblastoma cell lines compared to all other DepMap cell lines, measured by RNA-seq.

B. Like (A) but for *TOP2B*.

C. Waterfall plot showing Spearman correlations of the expression of all genes with CX-5461 sensitivity in GDSC neuroblastoma cell lines, with *TOP2A* and *TOP2B* highlighted in red and blue respectively.

D. Waterfall plot for the Spearman correlation of *TOP2B* expression with sensitivity ($1/IC_{50}$) of all drugs screened in GDSC neuroblastoma cell lines. CX-5461, etoposide and doxorubicin are highlighted in red, blue and green respectively.

E. Western blots for *TOP2A* (left) and *TOP2B* (right) following shRNA knockdown. CHP-134 cells were transduced with *TOP2A* or *TOP2B* shRNAs (2 shRNAs for *TOP2A* and 3 shRNAs for *TOP2B*). A control shRNA was used with scramble target in human cells. Cells were cultured in medium with 0.5 µg/ml puromycin and 2 µg/ml doxycycline for 3 days, then cell lysates were collected for western blotting. β-Actin was used as a loading control.

F. *TOP2A* (red) and *TOP2B* (blue) knockdown CHP-134 cells and negative control (black) cells were cultured in medium with 2 µg/ml doxycycline for 3 days, then, the indicated concentration of CX-5461, etoposide, doxorubicin or cisplatin was added to the medium for 72 hours. Cell viability was determined by MTS assay. Data represent mean ± SD of 3 independent experiments. ***$P < 0.001$.

G. *TOP2A* (red) and *TOP2B* (blue) knockdown CHP-134 cells and negative control (black) cells were cultured in medium with 2 µg/ml doxycycline for 3 days, then 0.05 µM (left) or 0.1 µM of CX-5461 was added to the medium for 0-4 days. Data represent mean ± SD of 3 independent experiments. **$P < 0.01$, ***$P < 0.001$.

H. Western blots for *TOP2A* (left) and *TOP2B* (right) following CRISPRa induced overexpression. CHP-134 cells were transduced with *TOP2A* or *TOP2B* gRNAs (2 gRNAs for each gene) or no gRNA control (dCas9-VPR). Cell lysates were collected for western blotting. β-Actin was used as a loading control.

I. *TOP2A* (red) and *TOP2B* (blue) overexpressing CHP-134 cells and negative control (black) cells were treated with the indicated concentration of CX-5461, etoposide, doxorubicin for 72 hours. Cell viability was determined by MTS assay. Data represent mean ± SD of 3 independent experiments.

J. Schematic of *in vitro* topoisomerase activity assay (decatenation assay) workflow.

K. Bar plot showing the drug concentration required to inhibit 25% of total DNA decatenation (IC_{25}) in an *in vitro* topoisomerase activity assay for a commercial CX-5461 stock, an additional CX-5461 stock that we synthesized, doxorubicin, etoposide and ciprofloxacin. The assay was repeated five times with the error bars representing 95% confidence intervals. Note: we calculated an IC_{25} because CX-5461 did not achieve a reliably measurable IC_{50} within the active drug concentration range for the TOP2A assay (see Fig. S4C).

L. Plot showing the relative difference in the concentration of each topoisomerase inhibitor (x-axis) required to inhibit the decatenation of kDNA in the presence of TOP2B relative to TOP2A (y-axis), calculated from the assays performed in panel K. Error bars represent 95% confidence intervals.

M. Bar plot showing the drug concentration required to inhibit 50% of total DNA relaxation (IC_{50}) for CX-5461, doxorubicin, etoposide and ciprofloxacin. The assay was run twice with repeat runs shown in the left and right panels.

Neuroblastoma patient tumors overexpress *TOP2B*.

Given our discovery of the mechanism responsible for CX-5461's robust selective killing of

neuroblastoma cell lines, we next sought to determine the potential of CX-5461 to treat

neuroblastoma patients. We began by using existing patient genomics datasets to interrogate

the *in vivo* activity of the drug target *TOP2B* and to investigate the fidelity of the cell line models

used to identify CX-5461. First, it was recently shown that embedding cell lines and patient

tumors in a low dimensional latent representation of gene expression data represents a viable

21

438   strategy to determine whether cancer cell lines recapitulate their tumor-of-origin. We applied this

439   approach[39] to the DepMap[40] and GDSC cancer cell lines, which showed that neuroblastoma cell

440   lines were among the most representative of their tumor-of-origin (81% correctly aligned; $P <$

441   2.2×10^{-16}, Fig. 5A-B; Fig. S5A), supporting the relevance of the cell line screening data as a

442   model of neuroblastoma patient tumor biology.

443   We next explored the *in vivo* activity of *TOP2B* in primary tumors using neuroblastoma patient

444   genomics data. We used an aggregated dataset of 88 diagnostic neuroblastoma tumors where

445   RNA-seq and whole-genome sequencing were available[41]. First, the expression of *TOP2B* in

446   neuroblastoma cell lines was well maintained in patient primary tumors (median expression

447   104.74 TPM in DepMap neuroblastoma cell lines and 132.4 TPM in our patient tumor cohort;

448   Fig. 5C left). This result was consistent when we normalized against the mean expression of

449   housekeeping genes actin *ACTB (ACTIN)* and *GAPDH* to account for dataset-specific effects

450   (Fig. 5C right). We next assessed the expression of *TOP2B* across TCGA tumor samples. As

451   was true for cell lines, *TOP2B* was more highly expressed in neuroblastoma tumors than other

452   cancers (Fig. 5D, Fig. S5B-C). We also interrogated expression data from relapsed[2] and

453   metastatic[42] neuroblastoma tumors, which had paired primary tumor data and we identified no

454   evidence of depletion of *TOP2B* expression in metastases or relapse (Fig. 5E-5F). Together,

455   these data are consistent with the high *TOP2B* expression in neuroblastoma cell lines being

456   maintained in patient tumors.

457   Notably, the expression of *TOP2B* varies over a 14.57-fold range in these patient tumors (min =

458   27.8 TPM, max = 405.2 TPM), implying that clinical studies of CX-5461 would benefit from

459   stratifying patients based on the expression of *TOP2B*, the primary drug target. To explore the

460   drivers of these differences, we interrogated the effect of 38 clinical variables and genomic

461   features on *TOP2B* expression. These included somatic mutations, mutation signatures, copy

462   number aberrations, and structural variants. Because of correlations among these features, we

22

463   used an ElasticNet regression model (α = 0.5) to determine which features were independently

464   predictive of *TOP2B* expression. The model identified 3 predictors; deletion of the 3p arm of

465   chromosome 3 (del(3p)), the q arm of chromosome 11 (del(11q)), and patient age-at-diagnosis

466   (Table S2). *TOP2B* is on chromosome 3p and as expected, del(3p) was associated with a 2-fold

467   decrease in its expression (Fig. 5G). Surprisingly, age-at-diagnosis was also a strong predictor

468   of *TOP2B* expression, with younger patients expressing much higher levels of *TOP2B* (Fig. 5H).

469   *TOP2B* expression was also associated with *MYCN* expression when we conditioned on del(p3)

470   and age-at-diagnosis using multivariate linear regression ($P = 3.3 \times 10^{-3}$). ChIP-seq data also

471   showed that MYCN is bound to the *TOP2B* promoter (Fig. S5D), consistent with the causal

472   relationship between CX-5461 IC_{50} and *MYCN* expression that we observed in cell lines (Fig.

473   1G). Overall, these genomics analyses of patient tumors suggest that high TOP2B activity is

474   maintained and may be therapeutically relevant in a subset of neuroblastoma patients. To

475   explore the potential for a CX-5461 therapeutic window in cancer patients, we also assessed

476   the expression of *TOP2B* in normal human tissues using data from the Genotype-Tissue

477   Expression (GTEx) consortium. Although the expression of *TOP2B* was again typically higher in

478   neuroblastoma tumors than normal human tissues (Fig. 5I), there was clear expression across

479   normal tissues, including cardiac tissues and most strikingly some regions of the brain (Fig.

480   S5E-S5F). These genomics analyses provide further confidence that CX-5461's selective

481   activity against neuroblastoma cell lines could translate to anti-neuroblastoma tumor activity *in*

482   *vivo. TOP2B*'s expression in normal tissues does, however, highlight potential patient safety

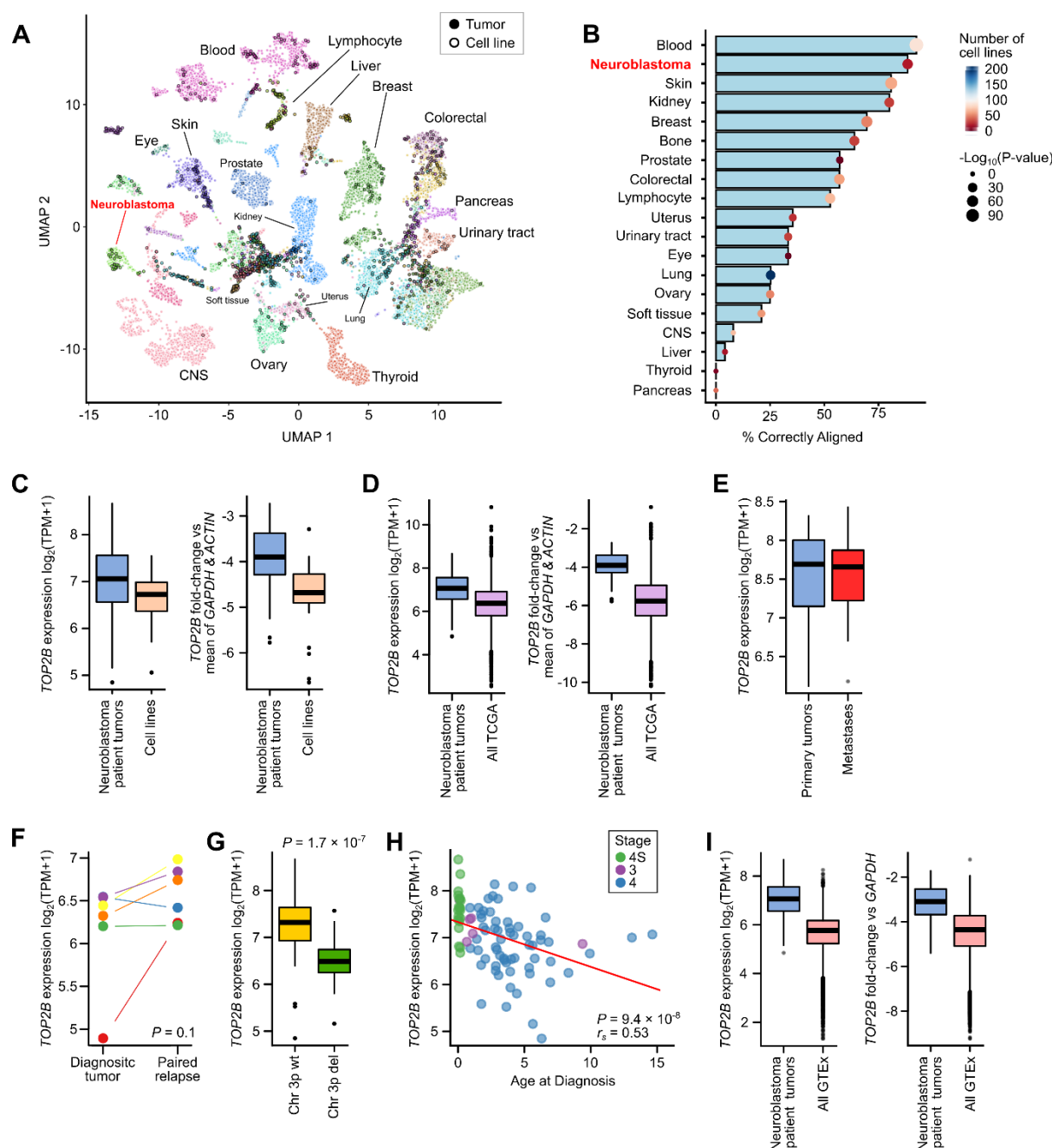483   concerns given the proposed CX-5461 mechanism-of-action.

23

Figure 5. *TOP2B* expression is similar in neuroblastoma patient tumors and cell lines, but it is also expressed in normal cells.

A. UMAP representation showing the genome-wide gene-expression-based alignment of all DepMap cell lines with patient tumor gene expression data from TCGA, Treehouse and TARGET, generated using the Celligner tool. The points representing individual cell lines have a black border. Points have been colored by their lineage and clusters have been labeled by tumor lineage.

B. The proportion of cell lines from a given lineage that correctly align with the appropriate patient tumor cluster (x-axis). The points have been colored by the number of cell lines in the datasets. The size of the points has been scaled by the *P*-value obtained from a Fisher's exact test for cluster membership.

24

494   C. Boxplot of *TOP2B* expression in neuroblastoma cell lines obtained from DepMap RNA-seq vs 88
495   neuroblastoma patient tumors for $\log_2(\text{TPM}+1)$ normalized RNA-seq expression (left) and *TOP2B*
496   expression in these datasets normalized to *ACTIN* and *GAPDH* housekeeping genes (right panel).

497   D. *TOP2B* RNA-seq expression data in 88 neuroblastoma patient tumors compared to all TCGA tumors for
498      $\log_2(\text{TPM}+1)$ normalized expression values (left) and *TOP2B* normalized to *ACTIN* and *GAPDH*
499   housekeeping genes (right).

500   E. *TOP2B* $\log_2(\text{TPM}+1)$ normalized expression at primary sites and metastatic sites in published RNA-seq
501   data obtained from Rifatbegovic *et al*.

502   F. *TOP2B* $\log_2(\text{TPM}+1)$ normalized RNA-seq expression obtained from 6 patients in the TARGET cohort for
503   whom both diagnostic and matched relapse tumor gene expression data were available.

504   G. Boxplot showing *TOP2B* $\log_2(\text{TPM}+1)$ normalized RNA-seq expression from 88 neuroblastoma patient
505   tumors with a chromosome 3p deletion compared to the wild-type (wt) copy of chromosome 3p.

506   H. Scatterplot of *TOP2B* $\log_2(\text{TPM}+1)$ normalized RNA-seq expression (y-axis) plotted against age (x-axis)
507   for 88 neuroblastoma patient tumors. Patients are colored by disease stage, with stage 4S, 3 and 4 patients
508   colored green, purple and blue respectively.

509   I. *TOP2B* RNA-seq expression data in 88 neuroblastoma patient tumors compared to all GTEx normal tissues
510   for $\log_2(\text{TPM}+1)$ normalized expression values (left) and *TOP2B* normalized to *ACTIN* and *GAPDH*
511   housekeeping genes as negative controls (right).

512

513 **CX-5461 synergizes with inhibitors of ATM, ATR, and TOP1.**

514 In the last decade, single-agent clinical trials in neuroblastoma have almost universally failed,

515 even when the rationale for a new compound has been substantive[4]. For such an aggressive

516 disease, identifying synergistic drug combinations is critical. To address this problem, we

517 leveraged our CRISPR screening data, reasoning that druggable proteins whose genetic

518 knockout synergizes with CX-5461 may allow us to narrow the enormous combinatorial search

519 space. For these analyses, we leveraged a previously assembled list of druggable genes[13].

520 Among the top druggable genes, whose knockout synergizes with CX-5461 in CHP-134 cells

521 were *ATM*, *ATR*, and *TOP1* (Fig. 6A-6B), all genes converging on DNA damage response.

522 Based on our mechanistic work showing the DNA damaging effects of CX-5461 and previous

523 observations of their efficacy in other cancers[43,44] we chose to investigate drugs targeting these

524 genes as potential combinations with CX-5461. Thus, we screened CHP-134, IMR-5, BE(2)-

525 M17, and KELLY neuroblastoma cell lines with the combination of CX-5461 and AZD-1390

526 (ATM inhibitor), AZD-6738 (ATR inhibitor), and SN-38 (the active metabolite of irinotecan; TOP1

527 inhibitor). We screened each of 12 cell line–drug combination pairs with a comprehensive 12 ×

528   12 matrix of drug concentrations, achieving this scale using high-throughput robotic handling.

529   We estimated regions of synergy using the Zero Interaction Potency (ZIP) model[45].

530   Encouragingly, we identified regions of synergy at pharmacologically relevant drug

531   concentrations in all 12 cell line-drug combinations (at a fold change of > 1.5 relative to the

532   expectation given an additive model, and $P < 0.01$, Fig. 6C-G; Fig. S6A-L). To confirm the

533   validity of the high-throughput screen, we tested several of these combinations using a

534   conventional MTS assay. In every case, the synergy detected by the MTS assay was consistent

535   with the high-throughput screen, with six representative examples shown in Fig. 6H. Thus, *ATM*,

536   *ATR,* and *TOP1* inhibitors represent promising combinations with CX-5461-targeted TOP2B

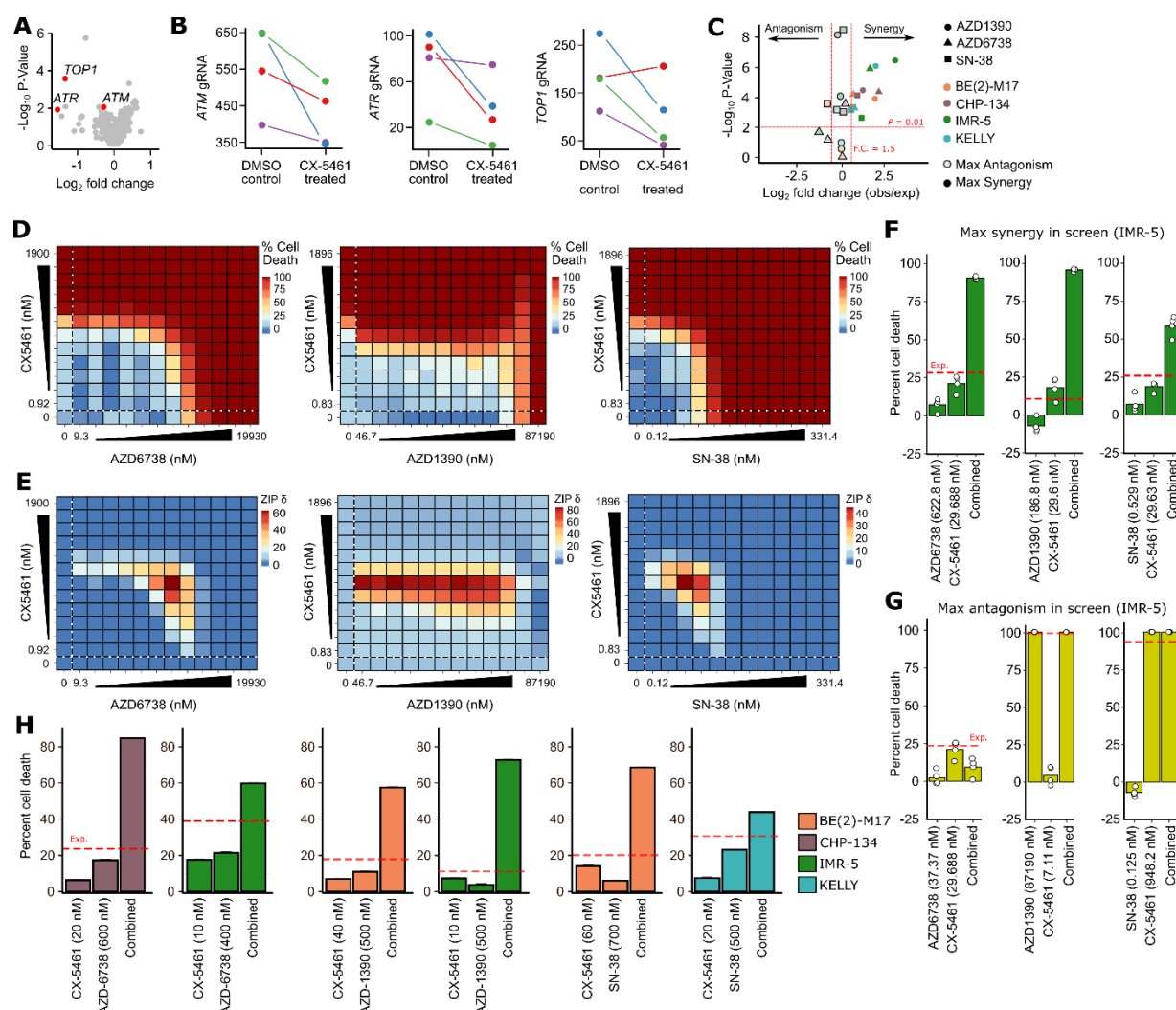537   inhibition to explore in preclinical *in vivo* studies.

Figure 6. CX-5461 synergizes with inhibitors of ATM, ATR and TOP1.

A. Sensitization of CHP-134 cells to CX-5461 following CRISPR knockout of known drug target genes (using a modified version of the list previously assembled by *Behan et al.*, 2019).

B. Normalized guide-RNA (gRNA) read counts (y-axis) for each of four independent guides used to knockout ATM (left), ATR (middle) and TOP1 (right).

C. Volcano plot depicting fold-changes (x-axis) and *P*-values (y-axis) at maximum synergy (unbordered shapes) and maximum antagonism (bordered shapes) scores observed in all 12 drug combination screening assays. The shape indicates which drug was combined with CX-5461 and the color of each point indicates the cell line screened. Fold-change is calculated relative to the expectation given additive drug activity and *P*-values were calculated using a one-sample t-test. Thresholds correspond to absolute $\log_2$(fold change) $\geq$ 1.5 and *P*-value $\leq$ .01.

D. Heatmap matrices of percent cell death in IMR-5 cells conferred by drug-only treatments (values within dotted lines) and combination treatments (all other values) for CX-5461 with AZD6738 (left), AZD1390 (middle), and SN-38 (right). Twelve-point doses were used at indicated concentrations with 1:2-fold dilutions for all compounds. Each matrix represents the average of four independent experiments. Data were normalized as a function of percent cell death according to inter-plate controls.

E. Heatmap matrices of synergy scores derived from respective cell death values in (D). All synergy was calculated based on the zero interaction potency (ZIP) model, and corresponding scores are shown as δ ZIP

27

557 according to the original method. Combinations conferring synergy or antagonism correspond to values
558 greater than or less than zero, respectively.
559 F-G. Bar plots of drug combinations that confer the maximum synergy (F) or maximum antagonism (G)
560 scores from their respective synergy calculations. White dots represent four independent experiments
561 corresponding to score maxima. Red dotted lines represent the expected result based on additivity alone.
562 H. Synergy validation with MTS assays for CX-5461 in combination with AZD6738, AZD1390, or SN-38.
563 Colors correspond to cell lines. Data are representative of 3 independent experiments.

564

565 **Establishing a pharmacologically relevant *in vivo* murine equivalent dosage for CX-5461.**

566 Given the selective activity of CX-5461 against neuroblastoma cell lines, the rational biological

567 mechanism, and the promising synergistic activity with other compounds *in vitro*, we sought to

568 perform an *in vivo* study to test these drug combinations in mice using orthotopic patient-derived

569 xenografts (PDX). To ensure the clinical relevance of our PDX data, we first performed

570 comprehensive *in vivo* preclinical pharmacokinetics studies, comparing CX-5461 plasma area

571 under the concentration-time curve (AUC) and average plasma concentration (Cavg) values to

572 those reported in the available human phase I clinical trial[15]. This is the first time such a study

573 has been reported for this compound. Notably, our PK results demonstrated highly variable CX-

574 5461 plasma concentrations in mice and revealed a much shorter terminal plasma half-life

575 compared to humans (83.3 hours in humans at 250 mg/m2 vs 3.7 hours after 5 mg/kg IV in

576 mice; Fig. S7A-C). This severely undermines the translational relevance of existing preclinical *in*

577 *vivo* CX-5461 studies in mice, which have not accounted for these differences. To mitigate

578 these issues we devised a low, multiple-dose CX-5461 regimen aimed at maintaining the Cavg

579 above 100 µg/L for 5 days, establishing a dosage of 5 mg/kg once daily by IP injection for 5

580 days, starting on day 1, with a second 5-day course starting on day 8, every 21 days.

581 We confirmed on-target drug activity *in vivo* at these pharmacologically relevant dosages using

582 TOP2cc formation and γ-H2AX as pharmacodynamic markers, interrogated using a RADAR

583 assay (Fig. 7A, Fig. S7D), and immunoblotting respectively (Fig. 7B), using PDX tumor tissue

584 harvested from CX-5461 treated mice. Consistent with our *in vitro* observations, we observed no

28

585 inhibition of RNA-POL I, but saw clear TOP2B trapping and DNA damage in these PDX tumors

586 following CX-5461 treatment (Fig. 7A-C), confirming the *in vivo* relevance of our mechanistic

587 work.

588

589 **CX-5461 improves survival *in vivo* when combined with TOP1 inhibitors in orthotopic**

590 **PDX mouse models.**

591 We performed our *in vivo* drug treatments using two luciferase-labeled PDXs—SJNBL046, a

592 *MYCN* amplified model from a 2-year-old male, and SJNBL047443, an ATRX mutant model

593 from a 12-year-old male. Both PDXs were from pre-treated neuroblastoma tumors, with

594 SJNBL046 surgically resected after induction chemotherapy and SJNBL047443 resected at

595 disease recurrence. We used RNA-seq to compare genome-wide gene expression in these

596 PDXs to their patient tumor of origin and the expression profiles were well maintained (r = 0.91,

597 P < 2.2 × 10^{-16} for SJNBL046; r = 0.75, P < 2.2 × 10^{-16} for SJNBL047443; Fig. 7D-E); *TOP2B*

598 expression was also maintained, suggesting these PDXs are a relevant disease model. We

599 implanted the cells by ultrasound-guided injection into the orthotopic para-adrenal region of

600 athymic-nude mice, and we monitored tumors using bioluminescent imaging and weekly

601 ultrasound (Fig. 7F-G; Fig. S7E-F).

602 We first tested 2-drug combinations of CX-5461 with pharmacologically relevant dosages of

603 AZD-1390 (ATMi), AZD-6738 (ATRi), and the liposomal formulation of the TOP1 inhibitor

604 irinotecan. We also tested 3-drug combinations involving CX-5461, irinotecan, and the ATMi or

605 ATRi (Fig. 7H). Combinations involving CX-5461 + ATMi had clear toxicity and were associated

606 with lower body weight (Fig. 7I; Fig. S7G). Indeed, for the CX-5461 + ATMi two-drug

607 combination, 30% (MYCN amplified group) and 36.8% (ATRX mutant group) of mice were

608 withdrawn (censored) from the study, primarily due to toxicity; this increased to 81.8% and

29

609   73.7% with the addition of irinotecan (Fig. 7J, Tables S3-S4). The combinations involving ATRi

610   lacked efficacy *in vivo*, with the two-drug combination of CX-5461 + ATRi showing no activity

611   beyond placebo, and no increase in efficacy was observed with the addition of ATRi to CX-5461

612   + irinotecan (Fig. 7J). However, the dual treatment of CX-5461 with the TOP1 inhibitor

613   irinotecan was effective, resulting in improved outcomes relative to placebo for both PDXs (P =

614   0.03 and P = 9.4 × 10^{-5} for MYCN and ATRX PDXs respectively; Tables S5-S6). Importantly, no

615   mice were censored due to toxicity.

616   We designed a second study to further explore the combination of CX-5461 with TOP1

617   inhibitors, combining CX-5461 with two 2-drug salvage combinations used in relapsed and

618   refractory neuroblastoma, which have been used as backbones for incorporating new agents in

619   clinical trials: irinotecan + temozolomide and topotecan + cyclophosphamide (Fig. 7K; Table S7-

620   S8)[46,47]. The therapies were reasonably tolerated with minimal loss of body weight (Fig. 7L; Fig.

621   S7H) or censoring (Figure 7M). For both regimens, the addition of CX-5461 improved outcome

622   in every group in both PDXs, clearest in the irinotecan + temozolomide combination in the

623   SJNBL047443 PDXs (P = 0.05; Tables S9-S10). Thus, in all six independent experiments, CX-

624   5461 improved survival when added to a TOP1 inhibitor (P = 0.01). The CX-5461 treated mice

625   also survived longer following cessation of therapy in all groups (mean 71 to 83.75 days and

626   90.8 to 144 days for the addition of CX-5461 to cyclophosphamide and topotecan, 21.75 to 24.8

627   days and 4 to 18.8 days for the addition of CX-5461 to irinotecan and temozolomide for the

628   MYCN and ATRX mutant PDX groups respectively; Table S7-S8).

629   Overall, our mouse studies suggest that combinations of CX-5461 with TOP1 inhibitors are

630   synergistic *in vivo* and have clinical potential in neuroblastoma. However, despite the anti-tumor

631   activity, our mechanistic work raises the possibility of late-emerging adverse events when

632   TOP2B is targeted, which needs to be further understood before this combination is applied in a
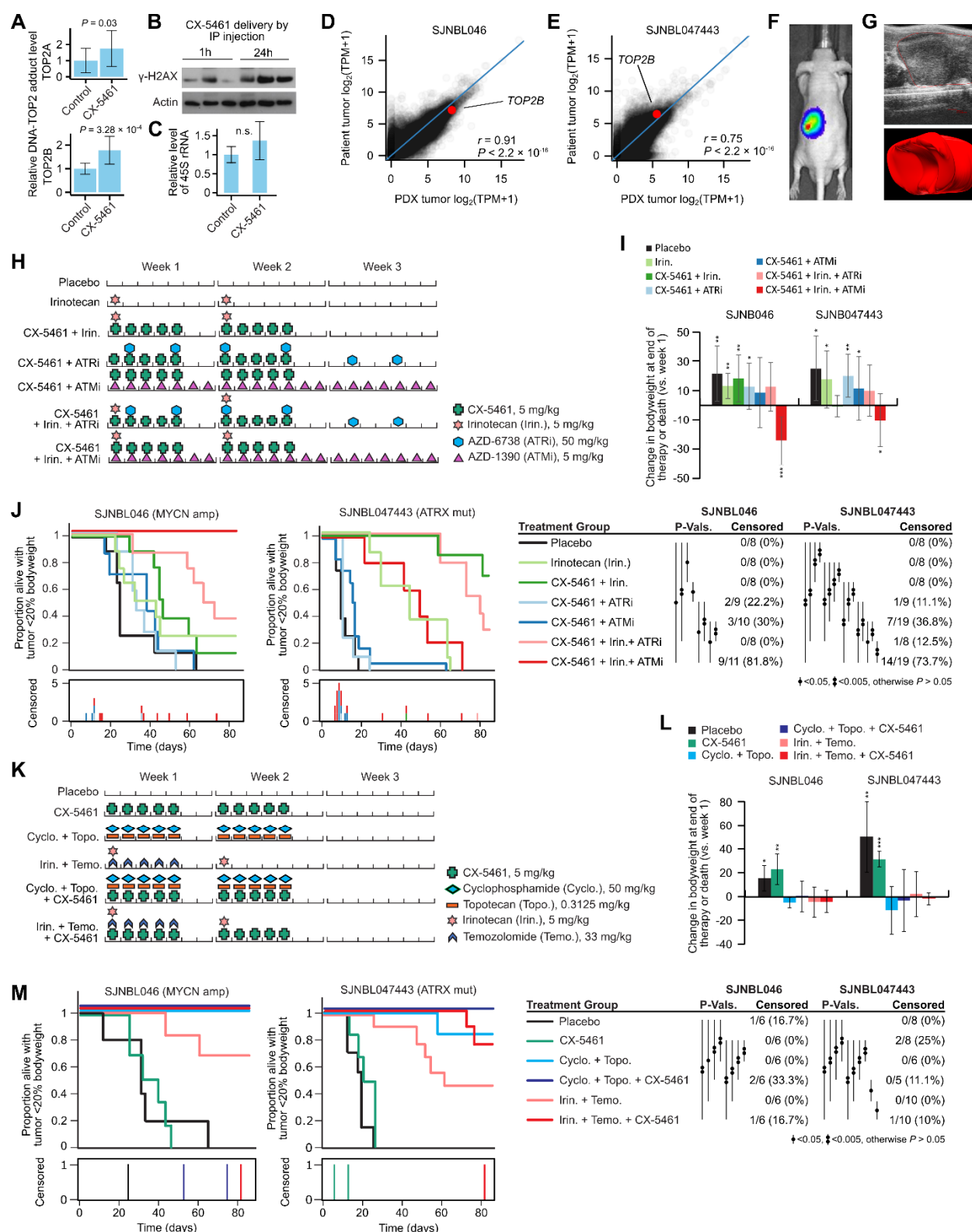
633   pediatric patient cohort.

Figure 7. CX-5461 shows promising anti-tumor activity in combination with TOP1 inhibitors *in vivo* using orthotopic PDX mouse models.

637   A. Bar plots showing quantified images from RADAR assay for TOP2-DNA adduct formation (y-axis) for
638   TOP2A (top panel) and TOP2B (bottom panel) in SJNBL046 PDXs harvested from CX-5461 treated mice
639   or control. Tissue for this experiment was obtained from our placebo and CX-5461 group in drug treatment
640   experiments (Fig. 7M). Data represent the mean ± SD of 12 replicates.
641   B. Western blots for γ-H2AX in tumor tissue obtained during PK study. Mice were treated with 25 mg/kg CX-
642   5461 by IP injection and tumors harvested at 1 h or 24 h. β-Actin was used as a loading control.
643   C. Bar plots showing the level of 45s rRNA, measured by qPCR, in the same tissue as Fig. 7A. Data represent
644   the mean ± SD of 12 replicates. n.s., no significant difference.
645   D. Genome-wide gene expression as measured by RNA-seq in *MYCN* amplified patient tumor SJNBL046 (y-
646   axis) and in the PDX derived from this tumor (x-axis). *TOP2B* is highlighted in red.
647   E. Same as (D) but showing data from the ATRX mutant sample SJNBL047443.
648   F-G. Representative image from tumor monitoring using luciferase bioluminescence imaging (F) and ultrasound
649   (G).
650   H. Drug combination schedule depicted for a single 3 weeks cycle in study 1. Mice were treated for 4 cycles.
651   I. Bar plot showing change of bodyweight for each group of mice at the end of therapy or at death (the mice
652   that died before completion of therapy) in study 1. Data represent the mean ± SD. *$P < 0.05$, **$P < 0.01$,
653   ***$P < 0.001$.
654   J. Kaplan-Meier curves showing the proportion of mice alive in each treatment group with a tumor burden
655   estimated at <20% of bodyweight, shown for SJNBL046 (left figure) and SJNBL047443 (right figure). The
656   number of mice censored in each treatment group at each time point is shown below. *P*-values were
657   calculated between pairs of curves using a log-rank test and are depicted by a vertical line, with the number
658   of dots corresponding to the level of significance; comparisons yielding $P > 0.05$ are not shown.
659   K. Drug combination schedule depicted for a single 3 weeks cycle in study 2. Mice were treated for 4 cycles.
660   L. Like (I) but showing bodyweights for study 2.
661   M. Like (J) but showing the results of study 2.

662

DISCUSSION

664   We used large-scale preclinical drug screening data to identify CX-5461 as exhibiting a

665   selective and reproducible cytotoxic effect in high-risk neuroblastoma and we discovered that

666   the primary target of CX-5461 at pharmacologically relevant concentrations is TOP2B. Because

667   of the functionally unique role of TOP2B, this finding completely alters the clinical trajectory of

668   CX-5461 in terms of patient stratification, rational combinations, potential resistance

669   mechanisms, and safety profile.

670   Evidence that CX-5461 inhibits the transcription of rRNA has fueled previous conclusions that

671   CX-5461 directly targets the RNA-POL I machinery[48]. Several studies have implicated CX-5461

672   as a binder of DNA G-quadruplexes *in vitro*[16,49], and a single systems biology study argued that

673   CX-5461 targets TOP2A[18] (TOP2B was not mentioned in ref. 18). However, none of these

32

674 previously proposed mechanisms of CX-5461 unify the wide range of observations made on this

675 compound—nor identified its molecular target. The activity of CX-5461 as a TOP2B inhibitor is

676 consistent with numerous previous observations, including CX-5461's DNA damaging effects[16]

677 and its tendency to inhibit RNA-POL I-mediated rRNA transcription[25], even in non-cycling cells

678 that do not express *TOP2A*[37]. Multiple previous studies have shown that topoisomerases play a

679 key role in resolving DNA topological issues to maintain active transcription[50], including at the

680 rRNA loci[51] and inhibition of topoisomerases (and treatment with topoisomerase inhibitors) has

681 been well established to cause inhibition of RNA-POL I[52,53]. Additionally, TOP2B has been

682 shown to localize to the rRNA locus, where RNA-POL I activity occurs[54]. Thus, our study leads

683 us to a parsimonious model, able to explain the capabilities of CX-5461 to induce DNA damage

684 and inhibit rDNA transcription: specifically, that the molecular target of CX-5461 is TOP2B, and

685 that previously observed inhibitory effects of CX-5461 on RNA-POL I are a consequence of

686 topoisomerase inhibition.

687

688 Interestingly *TOP2B* knockout mice die shortly after birth due to defects in the peripheral

689 nervous system occurring during the late stages of development[55], suggesting *TOP2B*'s

690 relevance as a drug target in neuroblastoma partially stems from the tumor's developmental

691 cell-of-origin. We showed that *TOP2B* remains overexpressed in neuroblastoma, particularly

692 younger and neonatal patients and that *TOP2B* expression is driven higher by *MYCN*

693 overexpression, explaining the selective activity of CX-5461 against neuroblastoma cells.

694 However, even though we showed anti-tumor activity in combination with TOP1 inhibitors *in vivo*

695 in orthotopic PDX models at pharmacologically relevant dosages, the clinical translation of CX-

696 5461 in neuroblastoma faces an unexpected obstacle—TOP2B as CX-5461's primary target

697 raises major previously unanticipated safety concerns. Existing TOP2A inhibitors can cause

698 serious *late-emerging* side effects, which would not be observable in a typical preclinical study,

33

699   nor the short-duration phase I clinical trial. For example, etoposide leads to therapy-induced

700   AML 2-3 years after treatment in about 1% of patients, and doxorubicin causes (frequently fatal)

701   cardiotoxicity in about 11% of patients, both of which are caused by off-target interactions with

702   TOP2B[20,21]. Consistent with this, our analysis of GTEx data showed that *TOP2B* is broadly and

703   highly expressed in normal human tissues, which is not true of *TOP2A*. CX-5461 has recently

704   been shown to be mutagenic in a *C. elegans* model[56], contradicting earlier claims that it is not

705   genotoxic[25]. Thus, our finding that CX-5461 primarily targets TOP2B provokes serious safety

706   concerns, and patients enrolled in ongoing CX-5461 phase II trials should be very closely

707   monitored for these late-emerging *TOP2B*-related adverse events. *TOP2B* is also particularly

708   highly expressed in the brain, thus blood-brain barrier penetration should be formally assessed.

709   Our analysis of TCGA data showed that subsets of both breast and hematological cancer

710   patients (the diseases of ongoing trials) also overexpress *TOP2B*, most strikingly in some

711   leukemias. Our identification of CX-5461's primary target will facilitate patient stratification in

712   these trials, which along with rational drug combinations will markedly improve the chances of

713   successful phase II trials in adult cancers, if safety concerns can be addressed. Indeed, given

714   the concerns surrounding the safety of TOP2B as a primary drug target, achieving promising

715   results in an adult cohort will likely be a prerequisite for a clinical study in children, where the

716   barriers to new clinical trials are much higher due to the limited and highly vulnerable patient

717   population.

718 **ACKNOWLEDGEMENTS**

725

726 **AUTHOR CONTRIBUTIONS**

727 P.G. conceived and directed the study. M.P. performed the experimental work. P.G. and M.P.

728 wrote the manuscript. P.G. and J.E. supervised the experimental work. C.W., R.C., M.S., A.Z.,

729 S.B., D.M., M.P., and P.G. performed computational work. J.B. and S.B. assisted with

730 topoisomerase activity assays. J.L. and S.C. performed drug screening, with C.W. analyzing the

731 data. Y.W. performed pharmacokinetic and bioanalytical assays, supervised by B.B.F. K.B.B.,

732 B.G., P.A. and E.S. performed the PDX experiments, directed by E.S. P.C. and S.M.P.M

733 assisted with CRISPR screening. J.B., S.N. and M.J.P. performed additional supportive

734 experimental work. R.K., M.M.B, M.A.D, J.S., T.C., L.A.G & S.B provided resources, insights

735 and supervised additional parts of the study. All authors edited the final manuscript.

736

737 **CONFLICTS OF INTERESTS**

738 The authors declare no competing interests.

739 **METHODS**

740 **Cell Lines and Cell Culture Conditions**

741 CHP-134, KELLY, and SK-N-SH cells were purchased from Sigma (MilliporeSigma, USA).

742 BE(2)-M17, SK-N_FI, RS4-11, H2452, and 293T cells were purchased from ATCC. IMR-5 cell

743 line was a gift from the Cellular Screening Center at the University of Chicago. IMR-5 was

744 cultured in Eagle's Minimum Essential Medium (EMEM, ATCC catalog# 30-2003) supplemented

745 with fetal bovine serum (FBS, ATCC® 30-2020™) to a final concentration of 10%. The rest of

746 the cell lines were cultured under conditions recommended by the vendors. All cells are cultured

747 at 37°C with 5% CO_2. No cell lines used in this study were found in the database of commonly

748 misidentified cell lines that is maintained by ICLAC and NCBI Biosample. Cell lines were tested

749 negative for mycoplasma using the MycoAlert mycoplasma detection kit (Lonza, LT07-118).

750 **Mice and Housing Conditions**

751 Athymic nude immunodeficient mice were purchased from Charles River (strain code 553). This

752 study was carried out in strict accordance with the recommendations in the Guide to Care and

753 Use of Laboratory Animals of the National Institute of Health. The protocol was approved by the

754 Institutional Animal Care and Use Committee at St. Jude Children's Research Hospital. All

755 efforts were made to minimize suffering. All mice were housed per approved IACUC protocols.

756 Animals were housed on a 12-12 light cycle (light on 6 am off 6 pm) and provided food and

757 water *ad libitum*.

758

36

Transfection and transduction

Inducible TRIPZ lentiviral shRNA of human TOP2A, TOP2B, and negative control shRNA plasmids were purchased from Dharmacon (Horizon Discovery, USA. TOP2A shRNA clone numbers are RHS4696-200686220, RHS4696-200769079. TOP2B clone numbers are RHS4696-200690242, RHS4696-200702560, RHS4696-200755958). MYCN shRNAs were ordered from Transomic Technologies (Cat# TLHSU2300-4613. Clone numbers are ULTRA-3327035, ULTRA-3327037, ULTRA-3475807). Lentiviral envelope and packing plasmids pMD2.G and psPAX2 were ordered from Addgene (pMD2.G #12259, psPAX2 #12260). To generate lentiviral particles, 293T cells were seeded in a 6-well plate one day before transfection. For one well of a 6-well plate, cells were co-transfected with 0.56 µg pMD2.G, 0.83 µg psPAX2, and 1.1 µg shRNA plasmid, using Lipofectamine 3000 (ThermoFisher, USA. Catalog# L3000008). Cell culture medium with lentivirus were collected three times during the time period 36 h to 72 h after transfection. CHP-134 cells were infected two to three times during 24 h. Two days after infection, 0.5 µg/ml puromycin was added to the culture medium to select infected positive cells. 2 µg/ml doxycycline was used to induce shRNA expression.

CRISPR activation sgRNA plasmids for TOP2A (Cat# GSGH11887-247255376, GSGH11887-247255378) and TOP2B (Cat# GSGH11887-247255386, GSGH11887-247255388), and plasmids for dCas9 expression (Cat# CAS11914) were ordered from Horizon Discovery. Lentiviral particles were generated with co-transfection with pMD2.G and psPAX2 in 293T cells. CHP-134 cells were infected with dCas9 lentivirus and dCas9-expressing CHP-134 cells were selected with 7 µg/ml blasticidin. The virus with TOP2A or TOP2B CRISPR activation sgRNAs were used to infect the blasticidin-resistant cells. Positive cells with TOP2A or TOP2B sgRNAs were selected with 0.5 µg/ml puromycin.

782 **RNA extraction and quantitative real-time RT-PCR**

783 Total RNA was extracted using Trizol (Invitrogen) according to the manufacturer's protocol.

784 cDNA was synthesized using qScript cDNA Synthesis Kit (Quanta Biosciences, catalog#

785 95047). SYBR Green PCR Master Mix (Quanta Biosciences, catalog# 95072-012) was used for

786 the quantitative real-time RT-PCR, which was performed on the CFX96 real-time PCR detection

787 system (Biorad). Experimental results were normalized to β-Actin. The primers for 45S pre-

788 rRNA internal transcribed spacer region and 18s rRNA were previously described [16] (45S-F 5'-

789 GCCTTCTCTAGCGATCTGAGAG-3', 45S-R 5'-CCATAACGGAGGCAGAGACA-3'; 18S-F 5'-

790 AAACGGCTACCACATCCA-3', 18S-R 5'-CCTCCAATGGATCCTCGT-3'). 28S-rRNA primers

791 were previously described [57] (28S-F 5'-GGGTGGTAAACTCCATCTAAGG-3', 28S-R

792 5'GCCCTCTTGAACTCTCTCTTC-3'). β-Actin-F 5'- CCAACCGCGAGAAGATGA -3', β-Actin-R

793 5'- CCAGAGGCGTACAGGGATAG -3'

794 **Flow cytometry**

795 For apoptosis, cells were treated in 6-well plates. After incubation for the time needed, cell

796 culture medium and cells were collected and washed in cold phosphate-buffered saline (PBS).

797 The cells were then resuspended in annexin-binding buffer and stained with Alexa Fluor 488

798 conjugated annexin V (Thermo Fisher, catalog# A13201) and 1 µg/ml Propidium iodide (PI) for

799 flow cytometry analysis. For cell cycle analysis, cells were fixed with cold 70% ethanol in water.

800 After 2× washes in PBS, cells were treated with 100 µg/ml RNase A and stained with 50 µg/ml

801 PI for flow cytometry analysis.

802

803

38

MTS and CellTiter-Glo assays

Cells were seeded in 96-well plates and treated with compounds as needed. Premixed MTS reagent (Abcam, ab197010) was added to the medium in a 96-well plate to a final concentration of 10%. Then the clear bottom plate was incubated in a cell culture incubator for 0.5 to 4 hours and absorbance was measured at 490nm. For CellTiter-Glo (Promega, G9241), reagent was added to the white bottom plate to a final concentration of 50%. The plate was then shaken for 2 min to induce cell lysis. After incubation at room temperature for 10 minutes, the luminescence was recorded.

Western blotting and band depletion assay

Generally, cells were washed with cold PBS and lysed in RIPA buffer (1% sodium deoxycholate, 0.1% SDS, 1% Triton X-100, 10 mM Tris [pH 8.0], and 150 mM NaCl) in cell culture plates. RIPA buffer was supplemented with Protease Inhibitor Cocktail (Sigma, #5892970001) and Phosphatase Inhibitor (Thermo Fisher, #A32957). For cleaved PARP detection, cell culture medium was also collected. Protein concentration was determined by BCA protein assay kit (Thermo Fisher, catalog# 23225). After boiled in 1× LDS sample buffer (Thermo Fisher, #NP0007), proteins were separated by SDS-PAGE and transferred to PVDF membranes. After blocking in 5% non-fat milk in TBS with 0.1% Tween-20, membranes were probed with primary antibodies and horseradish-peroxidase-conjugated secondary antibodies. The signal was visualized by Western Lightning Plus-ECL (PerkinElmer). Band-depletion assay was performed as previously described with slight modification [33]. Treated cells were lysed in culture plates with 1× Laemmli sample buffer (2% SDS, 10% glycerol, 0.002% bromphenol blue, 0.0625M Tris-Cl (pH 6.8), 10% 2-mercaptoethanol). Samples were boiled and 10 μl of each sample was separated by SDS-PAGE. The antibodies used for western blotting in this study are β-Actin

827 (Sigma, #A1978), cleaved PARP (Cells Signaling, #5625), TOP1 (Santa Cruz, #sc-271285),

828 TOP2A (Santa Cruz, #sc-365916), TOP2B (BD Biosciences, #611492), FLAG-Tag (Cell

829 Signaling, #2368), P53 (Santa Cruz, #sc-126), phospho-P53 S15 (Cell signaling, #9284),

830 pCHK1 S345 (Cell Signaling, #2348), CHK1 (Santa Cruz, #sc-8408), pCHK2 T68 (Cell

831 Signaling, #2661), CHK2 (Santa Cruz, #sc-17747), HRP-linked anti-rabbit IgG (Cell Signaling,

832 #7074), HRP-linked anti-mouse IgG (Cell Signaling, #7076).

833 **Immunofluorescence, EU and EdU incorporation**

834 Cells were seeded on poly-D-lysine coated coverslips before treatment. Treated cells were fixed

835 in 4% formaldehyde for 15-20 minutes and permeabilized with 0.3% Triton X-100 for 10 min at

836 room temperature. For γ-H2AX, 53BP1, and RPA staining, cells were blocked in 5% FBS/PBS

837 for 1 h at room temperature, then incubated with primary antibody diluted in 1% FBS/PBS

838 overnight at 4°C. Fluorochrome-conjugated secondary antibodies were incubated for 1 h at

839 room temperature. For G-quadruplex detection, RNA in fixed cells was digested by incubating

840 cells in 0.5 mg/ml RNase A for 1 h at 37°C. Then block coverslips with 0.5% goat serum in

841 PBST (PBS + 0.1% Tween20) for 1 h at 37°C. Primary antibody 1H6 (Millipore, # MABE1126)

842 was diluted in 0.5% goat serum/PBST and incubate with coverslips at 37°C for 1 hr or at 4°C

843 overnight. Alexa Fluor 488 conjugated secondary antibody was diluted in 0.5% goat

844 serum/PBST and incubate at room temperature for 1 h. ProLong® Gold Antifade Reagent with

845 DAPI (Cell Signaling, #8961) was used as coverslip mountant. Coverslips were mounted for 24

846 h at room temperature and subjected to fluorescence microscopy.

847 For ethynyl uridine (EU) and 5-ethynyl-2'-deoxyuridine (EdU) incorporation assay, Click-iT™

848 RNA Alexa Fluor™ 594 Imaging Kit (Thermo Fisher, #C10330) and Click-iT™ EdU Alexa

849 Fluor™ 488 Imaging Kit (Thermo Fisher, #C10337) were used. Experiments were carried out

40

850   following the manufacture's protocols. Briefly, cells were cultured in the medium with EU or EdU

851   for 30 min to 3 h. After fixation and permeabilization, cells were incubated for 30 minutes at

852   room temperature in EU or EdU Click-iT® reaction cocktail and then washed in Click‐iT®

853   reaction rinse buffer (for EU) or 3% BSA in PBS (for EdU). If needed, cells were processed for

854   additional staining as regular immunofluorescence.

855   Images were taken with the Nikon C2 confocal microscope and analyzed with NIS-Elements

856   Viewer imaging software. γ-H2AX signal were quantified and analyzed using ImageJ. The

857   antibodies used for immunofluorescence are γ-H2AX (Cell Signaling, #9718; Millipore, # 05-

858   636), 53BP1 (Abcam, ab36823), RPA (Millipore, # MABE285), Alexa fluor 488 conjugated goat

859   anti-mouse IgG (Thermo Fisher, #A-11001), Alexa fluor® 594 conjugate anti-rabbit IgG (Cell

860   Signaling, 8889).

861   **Comet assay**

862   Comet assay was performed with the Comet Assay Kit (Abcam, ab238544), following the

863   protocol from the manufacture. In brief, cells were collected and counted, then mixed with

864   Comet Agarose at 1/10 ratio (v/v). The cell and agarose mixture was immediately transferred

865   onto an agarose coated glass slide. After solidified at 4 °C for 15 min, the slide was incubated in

866   pre-chilled Lysis Buffer for 30-60 mins at 4ºC in the dark, then in pre-chilled Alkaline Solution for

867   30 mins at 4ºC in the dark. The slide was then subjected to electrophoresis in Alkaline Solution.

868   After fixed in 70% ethanol, DNA was stained with Vista Green DNA Dye. Slides were viewed

869   and imaged with Nikon C2 microscope at 10× magnification. Images were analyzed with

870   OpenComet tool.

871

872   **RADAR assay**

873   The assay was performed as previously described [34]. Treated cells were lysed with MB buffer

874   (6M guanidinium isothiocyanate, 10 mM Tris-HCl, pH 6.5, 20 mM EDTA, 4% Triton X100, 1%

875   Sarkosyl, and 1% dithiothreitol). Nucleic acids were precipitated by adding 100% ethanol to the

876   cell lysate to a final concentration of 33% (1/2 volume of the cell lysate). After 5 min of

877   incubation at -20 ºC, nucleic acids were collected by centrifugation. Pellet was washed with 75%

878   ethanol and dissolved in freshly made 8 mM NaOH solution. DNA concentration was

879   determined by NanoDrop 1000 spectrophotometer. 1 μg DNA from each sample was

880   transferred to a nitrocellulose membrane using the Bio-Dot SF microfiltration apparatus (Bio-

881   Rad, #170-6542). The membrane was blocked in 5% non-fat milk in TBS with 0.1% Tween-20,

882   then probed with primary antibodies and horseradish-peroxidase-conjugated secondary

883   antibodies. The signal was visualized by Western Lightning Plus-ECL (PerkinElmer). Antibodies

884   used were listed in section 'Western blotting and band depletion assays'.

885   **CRISPR screen**

886   CHP-134 cells were transduced with lentiCas9-Blast lentivirus. Media with 7 μg/ml blasticidin

887   was added 2 days later. After 5 days of selection, a single cell was seeded to each well of a 96-

888   well plate by flow cytometry single-cell sorting. Single clones were picked out after 3 weeks and

889   Cas9 expression level in each clone was determined by western blotting with Cas9 antibody

890   (Cell Signaling, #14697). Cas9 activity was tested using the CRISPRtest™ Functional Cas9

891   Activity Kit for Human Cells (Cellecta, #CRTEST). The clone with normal viability and high Cas9

892   activity (> 95%) was used for the following screening.

893   CHP-134 Cas9 cells were transduced at day 0 with lentiviral Brunello pooled library [58] at a low

894   MOI to make the transduction efficiency ~30% [59]. 0.5 μg/ml puromycin was used to select

895   transductants after 2 days of transduction (day 2). Cells were subcultured on day 4. On day 6,

896   cells were split into 2 groups, with 500 representatives for each gRNA in each group. On the

897   next day (day 7), one group of cells were treated with 0.04 µM CX-5461, DMSO was added to

898   the other group. All cells were collected for DNA extraction after 3 days (day 10).

899   The Brunello sgRNA pooled plasmid library (Addgene #73178) and lentiCas9-Blast plasmid

900   (Addgene #52962**)** were expanded following manufacturer's guidelines at The Center for

901   Advanced Genome Engineering at St. Jude Children's Research Hospital. Lentiviral particles

902   were generated by the St. Jude Vector Development and Production Core. Genomic DNA was

903   extracted using Nucleospin Blood XL kit (Macherey-Nagel cat# 740950) and eluted into 1ml

904   elution buffer. gDNA samples were amplified for next-generation sequencing at the St. Jude

905   Center for Advanced Genome Engineering using primer sets and reagent recommended by the

906   Broad Genetic Perturbation Platform (https://portals.broadinstitute.org/gpp/public/). Samples

907   were sequenced by the St. Jude Hartwell Center for Bioinformatics and Biotechnology and

908   resulting sequencing data analyzed using MAGeCK [60].

909   **Animal experiments**

910   Isolation of SJNBL046_X Cells: The tumor material was collected from a male patient

911   diagnosed with MYCN-amplified neuroblastoma at St. Jude Children's Research Hospital, after

912   informed consent and in agreement with local institutional ethical regulations.   Tumor tissue

913   was initially processed within 2 hours of surgical resection into a single cell suspension by

914   enzymatic dissociation and injected into the para-adrenal region of NSG mice using ultrasound

915   guidance as described below.   Tumor growth was monitored with ultrasound and manual

916   palpation. After tumor development, the tumor was harvested and passaged into athymic nude

917   mice using the same dissociation and ultrasound implantation techniques.

43

918   Isolation of SJNBL047443_X Cells: The tumor material was collected from a male patient

919   diagnosed with ATRX-mutated neuroblastoma at St. Jude Children's Research Hospital, after

920   informed consent and in agreement with local institutional ethical regulations.   Tumor tissue

921   was initially processed within 2 hours of surgical resection and implanted into the flank of an

922   NSG mouse. After tumor development, the tumor was harvested, processed into a single cell

923   suspension by enzymatic dissociation, and passaged into athymic nude in the para-adrenal

924   location using ultrasound guidance.

925   Orthotopic Ultrasound-Guided Para-adrenal Xenograft Implantation: All ultrasound procedures

926   were performed using the VEVO 3100 high-frequency ultrasound equipped with MS-MX250 24

927   MHz, MX550D 55 MHz, and MX700 70 MHz transducers (Fujifilm-Visualzonics, Toronto, ON,

928   Canada). Cells were suspended in Matrigel (BD Worldwide, Cat#354234) at a concentration of

929   2×10^4 cells per microliter and placed on ice. Anesthetized recipient athymic nude mice

930   (isoflurane 2-3% in 100% oxygen and delivered at 2 liters/min) were placed laterally on the

931   heated platform in right lateral recumbency. To provide a channel for delivery of the implant, a

932   22 gauge catheter (BD Worldwide, Cat# 381423) was gently inserted through the skin and back

933   muscle into the para-adrenal region, the stylet removed, and the hub clipped off. A chilled

934   Hamilton syringe fitted with a 27 gauge needle (1.5 inches) and loaded with 10 µl of the cell

935   suspension was inserted using a micromanipulator through the catheter and the tip positioned

936   between the kidney and adrenal gland via ultrasound guidance. The cell suspension was

937   injected into the region and the needle left in place for 30 seconds to permit the Matrigel

938   component to set before retracting the needle and catheter.

939   Statistical analysis: P-values for pairwise comparisons of all survival curves within each

940   experiment were calculated using a log-rank test, implemented in *survdiff()* function in the R

941   package "survival". Censoring plots and survival plots were created in R and Inkscape.

942

44

943   *Study 1*

944   Neuroblastoma orthotopic xenografts were created by injecting luciferase labeled SJNBL046_X

945   and SJNBL047443_X cells into recipient athymic nude mice using the para-adrenal injection

946   technique previously described. Mice were screened weekly by ultrasound for tumor volume

947   measurements. Mice were enrolled in the study when the tumor volume was the size of the

948   adrenal gland ($8mm^3$) or above and chemotherapy was started the following Monday.

949   SJNBL046_X mice (n = 64) and SJNBL047443_X mice (n=71) were randomized to 9 treatment

950   groups: liposomal irinotecan (Irin.), Irin. + CX-5461, Irin. + CX-5461 + AZD6738, Irin. + CX-5461

951   + AZD1390, CX-5461 + AZD1390, CX-5461 + AZD6738, and placebo. The following doses

952   were used:

953

TREATMENT GROUP	DOSING
Irin.	5 mg/kg once daily on days 1 and 8
Irin. + CX-5461	Irin. 5 mg/kg once daily on days 1 and 8, CX-5461 5 mg/kg once daily on days 1-5 and 8-12
Irin. + CX-5461 + AZD6738	Irin. 5 mg/kg once daily on days 1 and 8, CX-5461 5 mg/kg once daily on days 1-5 and 8-12, AZD6738 50 mg/kg once daily on days 2, 5, 9, 12, 16, and 19
Irin. + CX-5461 + AZD1390	Irin. 5 mg/kg once daily on days 1 and 8, CX-5461 5 mg/kg once daily on days 1-5 and 8-12, AZD1390 5 mg/kg once daily on days 1-21
CX-5461 + AZD1390	CX-5461 5 mg/kg once daily on days 1-5 and 8-12,

45

	AZD1390 5 mg/kg once daily on days 1-21
CX-5461 + AZD6738	CX-5461 5 mg/kg once daily on days 1-5 and 8-12, AZD6738 50 mg/kg once daily on days 2, 5, 9, 12, 16, and 19
PLACEBO	vehicle control (no chemotherapy)

954

955   *Study 2*

956   Neuroblastoma orthotopic xenografts were created by injecting luciferase labeled SJNBL046_X

957   and SJNBL047443_X cells into recipient athymic nude mice using the para-adrenal injection

958   technique previously described. Mice were screened weekly by ultrasound and tumor volume

959   was measured. Mice were enrolled in the study when the tumor volume was the size of the

960   adrenal gland ($8mm^3$) or above and chemotherapy was started the following Monday. Mice

961   received 4 courses of chemotherapy and ultrasound tumor volume was monitored between

962   courses and at the end of therapy. In addition to ultrasound, bioluminescence imaging was

963   performed weekly. Mice were monitored daily while receiving chemotherapy and removed from

964   the study and euthanized if found to be moribund at any time. Disease response was assigned

965   according to tumor size. Mice that did not have a tumor at the end of the study by ultrasound

966   and necropsy were classified as complete response. Mice that completed all 4 courses of

967   therapy and had a measurable tumor less than 20% of the bodyweight were classified as a

968   partial response. Mice with a tumor burden greater than 20% of the bodyweight at any point

969   were removed from the study and classified as progressive disease.

970   SJNBL046_X mice (n = 32) and SJNBL047443_X mice (n=44) were randomized to 6 treatment

971   groups: CX-5461, liposomal irinotecan (Irin.) + temozolomide (Temo.), cyclophosphamide

46

972 (Cyclo.) + topotecan (Topo.), Cyclo. + Topo. + CX-5461, Irin. + Temo. + CX-5461, and placebo.

973 The following doses were used:

974

TREATMENT GROUP	DOSING
CX-5461	5 mg/kg once daily on days 1-5 and 8-12
Irin. + Temo.	Irin. 5 mg/kg once daily on days 1 and 8, Temo. 33mg/kg once daily on days 1-5
Cyclo. + Topo.	Cyclo. 50 mg/kg once daily on days 1-5, Topo. 0.3125 mg/kg once daily on days 1-5
Cyclo. + Topo. + CX-5461	Cyclo. 50 mg/kg once daily on days 1-5, Topo. 0.3125 mg/kg once daily on days 1-5, CX-5461 5 mg/kg once daily on days 1-5 and 8-12
Irin. + Temo. + CX-5461	Irin. 5 mg/kg once daily on days 1 and 8, Temo. 33mg/kg once daily on days 1-5, CX-5461 5 mg/kg once daily on days 1-5 and 8-12
PLACEBO	vehicle control (no chemotherapy)

975

976 Abdominal Ultrasound and Tumor Volume Acquisition: The Vevo 3100 system was used for

977 ultrasound measurements of orthotopic neuroblastoma xenografts. Mice were anesthetized with

978 isoflurane (2%-3% in 100% oxygen) and positioned on the heated platform. The abdomen was

979 coated with ultrasound gel (Aquasonics, Parker Labs, Fairfield, NJ) and a MX250 or MX550

980 transducer used for 3D B-mode image acquisition. For volumetrics, 2D image slices were

47

981   acquired in the coronal plane covering a 20-30 mm range with a step-size of 0.076mm. All post-

982   processing of data was performed using Vevo LAB 3.2 software. Briefly, tumor margins were

983   manually segmented at 5-10 slice intervals, closed at the cranial and caudal ends and

984   reconstruction was performed to identify final volumes.

985   Bioluminescence Imaging and Quantification: Mice were anesthetized with isoflurane (2-3% in

986   100% oxygen) and bioluminescence images acquired with an IVIS Spectrum (Perkin Elmer,

987   Waltham, MA) 5 minutes after intraperitoneal injection of Potassium D-Luciferin solution (Perkin

988   Elmer, 3 mg/mouse). Luminescence values for all xenografts were quantified as the average

989   radiance (photons/s/cm2/sr) from identical regions of interest (ROI) encompassing the entire

990   abdomen using Living Image 4.7 (Perkin Elmer).

991

992   **Preclinical pharmacokinetic studies**

993   Previously published CX-5461 dosages in mice have ranged from 12-50 mg/kg orally (PO) or by

994   intraperitoneal (IP) injection, from once weekly to continuous 5-day on, 2-day off schedules [16,61–

995   64]. However, the pharmacokinetic (PK) profile of CX-5461 in mice has yet to be reported in

996   enough detail to judge the clinical relevance of such dosages and resultant plasma

997   concentrations. To determine a PK-guided clinically relevant dosage, we measured plasma and

998   tumor concentrations of CX-5461 in athymic nude mice at time points from 30 minutes to 24

999   hours after doses of 5 mg/kg IV and 25 mg/kg IP (Fig. S7A & S7B). We then compared CX-

1000   5461 plasma area under the concentration-time curve (AUC) and average plasma concentration

1001   (Cavg) values to those reported in the available human phase I clinical trial, which established a

1002   single agent maximum tolerated dose of 170 mg/m^2 by intravenous infusion [15]. We established a

1003   dosage of 5 mg/kg once daily by IP injection for 5 days, starting on day 1, with a second 5-day

1004   course starting on day 8, every 21 days. Our complete PK reports for all compounds screened

1005   in this study (including CX-5461) have been made freely available on the CSTN website

48

1006   (https://cstn.stjude.cloud/resources and

1007   https://www.stjude.org/content/dam/en_US/shared/www/research/cstn-appendix-standard-of-

1008   care-drug-regimens.pdf).

1009

1010   **Rescreen of GDSC cell lines with CX-5461**

1011   CX-5461 rescreening on a subset of GDSC cell lines was performed at the University of

1012   Chicago's Cellular Screening Center using the CellTiter Glo assay. We rescreened the IMR-5,

1013   CHP-134, KELLY, BE(2)-M17, SK-N-SH, SK-N-FI, RS4-11, and H2452 cell lines. Cells were

1014   plated in a 96-well plate for one day then drug treated in triplicate for 72 hours at 2-fold serial

1015   dilutions at 10 concentrations from 5 µM to 0.000 µM. Luminescence was quantitated using a

1016   standard plate reader and IC_{50} values were estimated using a generalized logistic regression

1017   model implemented in the "drc" package in R.

1018

1019   **High-throughput drug combination (synergy) screening**

1020   CX-5461 in combination with each of AZD6738, AZD1390, and SN-38 were dispensed into 384-

1021   well flat-bottom tissue culture-treated solid white plates (Corning, Catalog# 3570) using a

1022   Labcyte Echo 555 acoustic Liquid Dispenser (Beckman Coulter Life Sciences, USA). Twelve-

1023   point dose-response curves were generated using 1:2 dilution intervals for each drug. The top

1024   concentrations of the drugs were derived from pre-determined IC_{50} values and were as follows:

1025   311.4 nM SN-38, 1.89 µM CX-5461, 19.93 µM AZD6738, and 87.19 µM AZD1390. All plates

1026   contained two replicates each of the 144 pairwise combination matrices (all possible

1027   combinations of drug concentrations), the drugs alone without combination, DMSO-only (as a

1028   0% cell death control), and the maximum concentration of each drug combined (as a 100% cell

1029   death control). The final DMSO concentration of all wells was 0.536%. Each plate was

1030   generated twice for a total of four replicates per drug combination per cell line. Into the

49

1031 compound-containing plates, the neuroblastoma cell lines CHP-134 (2000 cells/well), KELLY

1032 (2250 cells/well), BE(2)-M17 (1750 cells/well), and IMR-5 (2750 cells/well) were plated in

1033 volumes of 40 μL using a Multidrop Combi reagent dispenser (ThermoFisher Scientific, USA)

1034 and settled for 20 seconds at 100x g in an Eppendorf 5810 centrifuge. Plates were then

1035 incubated at 37°C in 5% CO_2 for 96 hours in a Liconic STX220 incubator. Following incubation,

1036 plates were placed at room temperature for 20 minutes before viability assessment.   25 μL of

1037 CellTiter-Glo (Promega Catalog# G9241) was then added to each well to measure viability

1038 using a Multidrop Combi and the plates were incubated for an additional 25 minutes at room

1039 temperature. Luminescence was then detected with an EnVision 2102 Multilabel Plate Reader

1040 (PerkinElmer Life Sciences, USA).

1041

1042 **Drug synergy analysis**

1043 Raw luminescent data were imported into the R statistical environment version 4.0.2 (www.r-

1044 project.org). Background-subtracted values in raw luminescent units (RLU) were assigned to the

1045 appropriate drugs and concentrations, and each replicate was separated. All replicates were

1046 normalized to the mean of their respective inter-plate controls (DMSO for 0% cell death, and the

1047 maximum concentration of each drug combined for 100% cell death). Normalized drug-only data

1048 were fit with log-logistic regression to produce dose-response curves using the packages drc [65]

1049 and tidydrc (https://github.com/angelovangel/tidydrc). EC_{50} values for each drug's curve were

1050 extrapolated and plotted. Matrices of the percent cell death values were constructed using

1051 means of normalized data from each of the four replicates per group as input. From these

1052 normalized values, synergy scores were calculated for all tested concentration combinations.

1053 Delta scores derived from the Zero Interaction Potency (ZIP) model [45] were used to score

1054 synergy across all samples using the SynergyFinder package [66]. The most significant synergy

1055 (or antagonism) scores of drug pairs were directly compared to their corresponding single

1056 agents by referencing original normalized data of individual replicates and plotting mean values

50

1057   of percent cell death. From the resulting synergy matrices, both the highest- and lowest-scoring

1058   concentration pairs were extracted to represent the most significant synergy and antagonism,

1059   respectively. These scores were used to reference the expected percent cell death of a given

1060   combination (based on assumed non-interaction) to test whether the differences were

1061   statistically significant. *P*-values were calculated using a one sample t-test.

1062

1063   **TOP2A and TOP2B activity assays**

1064   Decatenation assay: 1 U of human topoisomerase II was incubated with 200 ng kDNA in a 30

1065   µl reaction at 37 C for 30 minutes under the following conditions: 50 mM Tris HCl (pH 7.5), 125

1066   mM NaCl, 10 mM MgCl2, 5 mM DTT, 0.5 mM EDTA, 0.1 mg/ml bovine serum albumin (BSA)

1067   and 1 mM ATP. Each reaction was stopped by the addition of 30 µl chloroform/iso-amyl alcohol

1068   (24:1) and 30 µl Stop Dye before being loaded on a 1.0% TAE gel run at 90V for 90 minutes.

1069   Bands were visualized by ethidium bromide staining for 15 minutes and destaining for 10

1070   minutes. Gels were scanned using documentation equipment (GeneGenius, Syngene,

1071   Cambridge, UK) and decatenation levels were calculated from band data obtained using

1072   ImageJ. A second individual also quantitated these images independently using different gel

1073   scanning software (GeneTools, Syngene, Cambridge, UK) and obtained similar results. The

1074   activity of the enzymes was determined before the testing of the compound. The amount of

1075   topoisomerase II required for optimal decatenation was determined by titration. The controls

1076   and compounds were tested over a range of dilutions from 1.734 µM to 400 µM and added to

1077   the reaction before the addition of the enzyme. Final DMSO concentration in the assays was

1078   10% (v/v). All experiments were performed five times and run on 1% agarose gels. Dose-

1079   response curves were estimated using a generalized logistic regression model fit to the data

1080   using the R package "drc", from which IC_{25}s and 95% confidence intervals were also calculated.

1081   Note that IC_{25}s were calculated because a measurable IC_{50} was not achieved within the active

1082   drug concentration range for CX-5461 in the TOP2A assays; to fit the dose-response curves

51

1083　　properly it was also necessary to filter those data, removing points beyond the activity range of

1084　　CX-5461.

1085

1086　　Relaxation Assays: 1 U of human topo II was incubated with 500 ng supercoiled pBR322 in a 30

1087　　µl reaction at 37 C for 30 minutes under the following conditions: 50 mM Tris HCl (pH 7.5), 125

1088　　mM NaCl, 10 mM MgCl2, 5 mM DTT, 0.5 mM EDTA, 0.1 mg/ml bovine serum albumin (BSA)

1089　　and 1 mM ATP. Each reaction was stopped by the addition of 30 µl chloroform/iso-amyl alcohol

1090　　(24:1) and 30 µl Stop Dye before being loaded on a 1.0% TAE gel run at 90V for 90 minutes.

1091　　Bands were visualized by ethidium bromide staining for 15 minutes and destaining for 10

1092　　minutes. Gels were scanned using documentation equipment (GeneGenius, Syngene,

1093　　Cambridge, UK) and relaxation levels were calculated from band data obtained with gel

1094　　scanning software (GeneTools, Syngene, Cambridge, UK). The data for all topoisomerase

1095　　activity assays were generated by Inspiralis (Innovation Centre, Norwich Research Park, Colney

1096　　Lane, Norwich, UK) and the experimental details above were provided by Inspiralis. The data

1097　　were analyzed by Inspiralis and reanalyzed by M.P and P.G, achieving consistent results.

1098

1099　　**Ligand docking and molecular dynamics simulations**

1100　　Published crystal structures of etoposide-bound TOP2A (PDB: 5GWK) or TOP2B (PDB: 3QX3)

1101　　were loaded into Maestro software (Schrödinger Release 2020-3). To prepare the protein for

1102　　docking and simulations, the protein preparation wizard was used to assign bond orders, add

1103　　hydrogens, create zero-order bonds to metals, create disulfide bonds, and fill in missing side

1104　　chains and loops. Default parameters were used for the optimization of hydrogen-bond

1105　　assignment (sampling of water orientations and use of pH 7.0). Waters beyond 5 Å of het

1106　　groups or with fewer than three hydrogen bonds to non-waters were removed. Restrained

1107　　energy minimization was applied using the OPLS3e forcefield. Prepared protein systems were

1108　　further checked by Ramachandran plots, ensuring there were no steric clashes.

1109

1110   For docking CX-5461 into TOP2A and TOP2B, the 3D structure of CX-5461 was first obtained

1111   from the PubChem database (www.pubchem.ncbi.nlm.nih.gov). The flexible ligand alignment

1112   tool in Maestro was used to align the core scaffold of CX-5461 to etoposide based on common

1113   scaffolds defined by the Bermis-Murcko method. The aligned molecule was then translated into

1114   the etoposide bound site based on these aligned scaffolds. The ligand position was adjusted in

1115   the binding site so that CX-5461 would occupy the optimal volume of the site through rigid body

1116   minimization of CX-5461 using Prime. The Prime tool was further used to adjust protein

1117   sidechain rotamers of TOP2A and TOP2B that are within 5 Å of CX-5461. The binding site was

1118   further optimized by administering a conjugate-gradient minimization algorithm for all residues

1119   within 5 Å of CX-5461, with a 200kcal/mol/Å^2 restraint placed on a shell of residues greater than

1120   5 Å but less than 7 Å from CX-5461. All atoms greater than 7 Å from CX-5461 were ignored by

1121   the algorithm.

1122

1123   For molecular dynamics simulations, systems were built for CX-5461-bound TOP2A and

1124   TOP2B by using the system builder panel of Desmond (Schrödinger Release 2020-3). The SPC

1125   solvent model was used, and the forcefield was set to OPLS3e. Solvated systems were loaded

1126   into the workspace by using the molecular dynamics panel. The total simulation time for each

1127   system was set to 10 nanoseconds, with 100-picosecond trajectory recording intervals. The

1128   system energy was set to 1.2, and the ensemble class used was NPT. Simulations were set to

1129   run at 300.0 K and 1.01325 bar. The option to relax model systems before simulations was

1130   selected.

1131

1132   Simulations were clustered based on RMSD using default parameters in the trj_cluster.py

1133   command line script available in Schrodinger utilities. This resulted in 12 clusters for TOP2A

1134   and 16 clusters for TOP2B. For each cluster, the representative structure file was used to

53

1135   calculate the relative binding affinity of TOP2A and TOP2B to the CX-5461 ligand. The binding

1136   energy was calculated using the Prime MM-GBSA tool from the Maestro GUI. The population of

1137   each cluster was used to determine weights for calculating a weighted average binding energy

1138   for TOP2A and TOP2B with CX-5461 from each of the clusters of the trajectory.

1139

1140   **Cell line drug screening analysis**

1141   Preprocessed GDSC data (drug sensitivity, gene expression, and mutation calls) were obtained

1142   from the GDSC website (www.cancerrxgene.org). All analyses of these data were performed

1143   using R and figures were created using the base graphics functions and the ggplot2 package.

1144   Basic statistical tests such as t-tests, linear regression, Wilcoxon-rank sum tests, and correlation

1145   tests were performed using the base statistical functions in R and, where appropriate, *P*-values

1146   were corrected for multiple testing by estimating false-discovery rates using the Benjamini and

1147   Hochberg method. The PRISM drug screening data were obtained from www.depmap.org.

1148

1149   **Patient *-omics* data analysis**

1150   Neuroblastoma patient tumor data was obtained from [41] who aggregated data from multiple

1151   previously published neuroblastoma studies including RNA-seq, clinical annotations, and

1152   genomics sequencing data. The associations between *TOP2B* expression and individual

1153   genomic and clinical features were estimated using linear regression. Sparse regression

1154   models, aimed at identifying independent predictors of *TOP2B* expression were fit using

1155   ElasticNet regression, implemented in the R package *glmnet*, where the alpha parameter was

1156   fixed to 0.5 and the lambda parameter was deduced by 10-fold cross-validation. GTEx data

1157   were obtained from the GTEx data portal (www.gtexportal.org), TCGA data from the Genomics

1158   Data Commons, paired relapse data was obtained from TARGET [67] and data from paired

1159   primary tumor and metastatic sites was obtained from [42]. Paired patient tumor – PDX gene

1160   expression data for our 2 xenografts was obtained from the St. Jude Cloud [68]. When comparing

54

1161   the expression of *TOP2B*, we also normalized these gene expression data by calculating their

1162 $\log_2$ fold-change relative to housekeeping genes *ACTIN* and *GAPDH*, which are treated as

1163   negative controls whose expression is not expected to vary, thus mitigating the effect of gene

1164   expression differences that would be expected to arise due to dataset-specific effects.

1165

1166   **Computational alignment of cell lines and tumor samples**

1167   To align cell lines to their corresponding lineages of patient tumor samples, the Celligner tool [39]

1168   was used. Clinical expression data were obtained from the UCSC Xena data hub

1169   (www.xena.ucsc.edu), which included processed data for tumor samples originating from The

1170   Cancer Genome Atlas (TCGA, www.cancer.gov) and TARGET (www.ocg.cancer.gov) datasets.

1171   Cell line expression data were obtained from Expression Atlas (www.ebi.ac.uk), which included

1172   RNA-sequencing of cell lines used in the Sanger Genomics of Drug Sensitivity in Cancer

1173   (GDSC, www.cancerrxgene.org) project. All expression data were in units of $\log_2$(TPM+1) and

1174   datasets were filtered such that only common lineages between tumors and cell lines were kept

1175   and used as input. After completion of the Celligner tool and the resulting UMAP plot was

1176   generated, alignments of cell lines to tumors were quantified by their respective lineages.

1177   Briefly, Celligner-generated tumor clusters were isolated and kept if they represented ≥ 80% of

1178   a given lineage. Proportions of cell lines that correctly aligned to their tumor counterpart clusters

1179   (by lineage) were then calculated. Fisher exact tests were performed to assess statistical

1180   significance for all alignments, and the resulting *P*-values and odds ratios were generated for

1181   each lineage. Step-by-step details of the Celligner tool, post-alignment analysis, and all input

1182   data are available in the Open Science Framework (www.osf.io/pzke4).

1183

1184   **Materials availability**

1185   PDX models that were used in this study are freely available upon request from the Childhood

1186   Solid Tumor Network (CSTN), which is hosted at St. Jude

55

1187   (https://www.stjude.org/research/resources-data/childhood-solid-tumor-network/available-

1188   resources.html). We have also made the full detailed pharmacokinetic reports for the

1189   compounds used in our PDX studies (including CX-5461) available on the CSTN website

1190   (https://cstn.stjude.cloud/resources and

1191   https://www.stjude.org/content/dam/en_US/shared/www/research/cstn-appendix-standard-of-

1192   care-drug-regimens.pdf).

1193

1194   **Data and code availability**

1195   The code to reproduce computational analyses in this study, including the supporting data, have

1196   been deposited on Open Science Framework (osf.io/pzke4/).

1197

REFERENCES

1. Louis, C. U. & Shohet, J. M. Neuroblastoma: Molecular pathogenesis and therapy. *Annu. Rev. Med.* (2015). doi:10.1146/annurev-med-011514-023121

2. Ma, X. *et al.* Pan-cancer genome and transcriptome analyses of 1,699 paediatric leukaemias and solid tumours. *Nature* **555**, 371–376 (2018).

3. Wedekind, M. F., Denton, N. L., Chen, C.-Y. & Cripe, T. P. Pediatric Cancer Immunotherapy: Opportunities and Challenges. *Pediatr. Drugs* **20**, 395–408 (2018).

4. Moreno, L. *et al.* Accelerating drug development for neuroblastoma: Summary of the Second Neuroblastoma Drug Development Strategy forum from Innovative Therapies for Children with Cancer and International Society of Paediatric Oncology Europe Neuroblastoma. *Eur. J. Cancer* **136**, 52–68 (2020).

5. Barretina, J. *et al.* The Cancer Cell Line Encyclopedia enables predictive modelling of anticancer drug sensitivity. *Nature* **483**, 603–7 (2012).

6. Garnett, M. J. *et al.* Systematic identification of genomic markers of drug sensitivity in cancer cells. *Nature* **483**, 570–5 (2012).

7. Stewart, E. *et al.* Targeting the DNA repair pathway in Ewing sarcoma. *Cell Rep.* **9**, 829–41 (2014).

8. Federico, S. M. *et al.* A phase I trial of talazoparib and irinotecan with and without temozolomide in children and young adults with recurrent or refractory solid malignancies. *Eur. J. Cancer* **137**, 204–213 (2020).

9. Kim, K. H. & Roberts, C. W. M. Targeting EZH2 in cancer. *Nat. Med.* **22**, 128–34 (2016).

10. Durbin, A. D. *et al.* Selective gene dependencies in MYCN-amplified neuroblastoma include the core transcriptional regulatory circuitry. *Nat. Genet.* **50**, 1240–1246 (2018).

57

1221   11.   Puissant, A. *et al.* Targeting MYCN in neuroblastoma by BET bromodomain inhibition.

1222   *Cancer Discov.* **3**, 308–23 (2013).

1223   12.   Corsello, S. M. *et al.* Discovering the anti-cancer potential of non-oncology drugs by

1224   systematic viability profiling. *Nat. cancer* **1**, 235–248 (2020).

1225   13.   Behan, F. M. *et al.* Prioritization of cancer therapeutic targets using CRISPR–Cas9

1226   screens. *Nature* **568**, 511–516 (2019).

1227   14.   Francies, H. E., McDermott, U. & Garnett, M. J. Genomics-guided pre-clinical

1228   development of cancer therapies. *Nat. Cancer* **1**, 482–492 (2020).

1229   15.   Khot, A. *et al.* First-in-Human RNA Polymerase I Transcription Inhibitor CX-5461 in

1230   Patients with Advanced Hematological Cancers: Results of a Phase I Dose Escalation

1231   Study. *Cancer Discov.* CD-18-1455 (2019). doi:10.1158/2159-8290.CD-18-1455

1232   16.   Xu, H. *et al.* CX-5461 is a DNA G-quadruplex stabilizer with selective lethality in BRCA1/2

1233   deficient tumours. *Nat. Commun.* **8**, 14432 (2017).

1234   17.   De Magis, A. *et al.* DNA damage and genome instability by G-quadruplex ligands are

1235   mediated by R loops in human cancer cells. *Proc. Natl. Acad. Sci. U. S. A.* 201810409

1236   (2018). doi:10.1073/pnas.1810409116

1237   18.   Bruno, P. M. *et al.* The primary mechanism of cytotoxicity of the chemotherapeutic agent

1238   CX-5461 is topoisomerase II poisoning. *Proc. Natl. Acad. Sci. U. S. A.* (2020).

1239   doi:10.1073/pnas.1921649117

1240   19.   Austin, C. A. *et al.* TOP2B: The First Thirty Years. *Int. J. Mol. Sci.* **19**, (2018).

1241   20.   Cowell, I. G. *et al.* Model for MLL translocations in therapy-related leukemia involving

1242   topoisomerase IIβ-mediated DNA strand breaks and gene proximity. *Proc. Natl. Acad.*

1243   *Sci. U. S. A.* **109**, 8989–94 (2012).

58

1244   21.   Zhang, S. *et al.* Identification of the molecular basis of doxorubicin-induced cardiotoxicity.

1245   *Nat. Med.* **18**, 1639–42 (2012).

1246   22.   Iorio, F. *et al.* A Landscape of Pharmacogenomic Interactions in Cancer. *Cell* **166**, 740–

1247   754 (2016).

1248   23.   Liu, X., Turbyville, T., Fritz, A. & Whitesell, L. Inhibition of insulin-like growth factor I

1249   receptor expression in neuroblastoma cells induces the regression of established tumors

1250   in mice. *Cancer Res.* **58**, 5432–8 (1998).

1251   24.   Khot, A. *et al.* First-in-Human RNA Polymerase I Transcription Inhibitor CX-5461 in

1252   Patients with Advanced Hematologic Cancers: Results of a Phase I Dose-Escalation

1253   Study. *Cancer Discov.* **9**, (2019).

1254   25.   Bywater, M. J. *et al.* Inhibition of RNA Polymerase I as a Therapeutic Strategy to Promote

1255   Cancer-Specific Activation of p53. *Cancer Cell* **22**, 51–65 (2012).

1256   26.   Olivieri, M. *et al.* A Genetic Map of the Response to DNA Damage in Human Cells. *Cell* **0**,

1257   (2020).

1258   27.   Ledesma, F. C., El Khamisy, S. F., Zuma, M. C., Osborn, K. & Caldecott, K. W. A human

1259   5′-tyrosyl DNA phosphodiesterase that repairs topoisomerase-mediated DNA damage.

1260   *Nature* **461**, 674–678 (2009).

1261   28.   Morimoto, S. *et al.* Type II DNA Topoisomerases Cause Spontaneous Double-Strand

1262   Breaks in Genomic DNA. *Genes (Basel).* **10**, (2019).

1263   29.   Crawford, L. J., Anderson, G., Johnston, C. K. & Irvine, A. E. Identification of the APC/C

1264   co-factor FZR1 as a novel therapeutic target for multiple myeloma. *Oncotarget* **7**, 70481–

1265   70493 (2016).

1266   30.   Haddach, M. *et al.* Discovery of CX-5461, the first direct and selective inhibitor of RNA

1267   polymerase I, for cancer therapeutics. *ACS Med. Chem. Lett.* **3**, 602–6 (2012).

1268 31. Levine, C., Hiasa, H. & Marians, K. J. DNA gyrase and topoisomerase IV: biochemical

1269   activities, physiological roles during chromosome replication, and drug sensitivities.

1270   *Biochim. Biophys. Acta - Gene Struct. Expr.* **1400**, 29–43 (1998).

1271 32. Liang, X. *et al.* A comprehensive review of topoisomerase inhibitors as anticancer agents

1272   in the past decade. *Eur. J. Med. Chem.* **171**, 129–168 (2019).

1273 33. Kaufmann, S. & Svingen, P. Immunoblot analysis and band depletion assays. *Methods*

1274   *Mol. Biol.* **94**, (1999).

1275 34. Kiianitsa, K. & Maizels, N. A rapid and sensitive assay for DNA-protein covalent

1276   complexes in living cells. *Nucleic Acids Res.* **41**, e104 (2013).

1277 35. Tammaro, M., Barr, P., Ricci, B. & Yan, H. Replication-dependent and transcription-

1278   dependent mechanisms of DNA double-strand break induction by the topoisomerase 2-

1279   targeting drug etoposide. *PLoS One* **8**, e79202 (2013).

1280 36. Nitiss, J. L. Targeting DNA topoisomerase II in cancer chemotherapy. *Nat. Rev. Cancer*

1281   **9**, 338–350 (2009).

1282 37. Prakash, V. *et al.* Ribosome biogenesis during cell cycle arrest fuels EMT in development

1283   and disease. *Nat. Commun.* **10**, 2110 (2019).

1284 38. Hsiao, C. J. *et al.* Characterizing and inferring quantitative cell cycle phase in single-cell

1285   RNA-seq data analysis. *Genome Res.* **30**, 611–621 (2020).

1286 39. Warren, A. *et al.* Global computational alignment of tumor and cell line transcriptional

1287   profiles. *bioRxiv* 2020.03.25.008342 (2020). doi:10.1101/2020.03.25.008342

1288 40. Tsherniak, A. *et al.* Defining a Cancer Dependency Map. *Cell* **170**, 564-576.e16 (2017).

1289   41.   Brady, S. W. *et al.* Pan-neuroblastoma analysis reveals age- and signature-associated

1290   driver alterations. *Nat. Commun.* **11**, 5183 (2020).

1291   42.   Rifatbegovic, F. *et al.* Neuroblastoma cells undergo transcriptomic alterations upon

1292   dissemination into the bone marrow and subsequent tumor progression. *Int. J. cancer*

1293   **142**, 297–307 (2018).

1294   43.   Negi, S. S. & Brown, P. Transient rRNA synthesis inhibition with CX-5461 is sufficient to

1295   elicit growth arrest and cell death in acute lymphoblastic leukemia cells. *Oncotarget* **6**,

1296   34846–58 (2015).

1297   44.   Yan, S. *et al.* Targeting RNA Polymerase I transcription synergises with TOP1 inhibition

1298   in potentiating the DNA damage response in high-grade serous ovarian cancer. *bioRxiv*

1299   849307 (2019). doi:10.1101/849307

1300   45.   Yadav, B., Wennerberg, K., Aittokallio, T. & Tang, J. Searching for Drug Synergy in

1301   Complex Dose-Response Landscapes Using an Interaction Potency Model. *Comput.*

1302   *Struct. Biotechnol. J.* **13**, 504–13 (2015).

1303   46.   Federico, S. M. *et al.* A Pilot Trial of Humanized Anti-GD2 Monoclonal Antibody

1304   (hu14.18K322A) with Chemotherapy and Natural Killer Cells in Children with

1305   Recurrent/Refractory Neuroblastoma. *Clin. Cancer Res.* **23**, 6441–6449 (2017).

1306   47.   DuBois, S. G. *et al.* Phase II Trial of Alisertib in Combination with Irinotecan and

1307   Temozolomide for Patients with Relapsed or Refractory Neuroblastoma. *Clin. Cancer*

1308   *Res.* **24**, 6142–6149 (2018).

1309   48.   Hein, N., Hannan, K. M., D'Rozario, J. & Hannan, R. Inhibition of Pol I Transcription a

1310   New Chance in the Fight Against Cancer. *Technol. Cancer Res. Treat.* **16**, 736–739

1311   (2017).

1312   49.   Wang, Y. *et al.* G-quadruplex DNA drives genomic instability and represents a targetable

1313   molecular abnormality in ATRX-deficient malignant glioma. *Nat. Commun.* **10**, 943

1314   (2019).

1315   50.   Pommier, Y., Sun, Y., Huang, S. N. & Nitiss, J. L. Roles of eukaryotic topoisomerases in

1316   transcription, replication and genomic stability. *Nat. Rev. Mol. Cell Biol.* **17**, 703–721

1317   (2016).

1318   51.   Zhang, H., Wang, J. C. & Liu, L. F. Involvement of DNA topoisomerase I in transcription

1319   of human ribosomal RNA genes. *Proc. Natl. Acad. Sci. U. S. A.* **85**, 1060–4 (1988).

1320   52.   Zimmer, C. Nicholas R. Cozzarelli and James C. Wang (Editors), DNA Topology and Its

1321   Biological Effects (Monograph 20). 480 S., 63 Abb., 10 Tab. Cold Spring Harbor 1990.

1322   Cold Spring Harbor Laboratory ISBN: 0–87969–348–7. $ 97.00. *J. Basic Microbiol.* **31**,

1323   328–328 (1991).

1324   53.   Burger, K. *et al.* Chemotherapeutic drugs inhibit ribosome biogenesis at various levels. *J.*

1325   *Biol. Chem.* **285**, 12416–25 (2010).

1326   54.   Uusküla-Reimand, L. *et al.* Topoisomerase II beta interacts with cohesin and CTCF at

1327   topological domain borders. *Genome Biol.* **17**, 182 (2016).

1328   55.   Yang, X., Li, W., Prescott, E. D., Burden, S. J. & Wang, J. C. DNA topoisomerase IIbeta

1329   and neural development. *Science* **287**, 131–4 (2000).

1330   56.   Ye, F. B. *et al.* Characterization of the phototoxicity, chemigenetic profile, and mutational

1331   signatures of the chemotherapeutic CX-5461 in Caenorhabditis elegans. *bioRxiv*

1332   2019.12.20.884981 (2019). doi:10.1101/2019.12.20.884981

1333   57.   Hald, Ø. H. *et al.* Inhibitors of ribosome biogenesis repress the growth of MYCN-amplified

1334   neuroblastoma. *Oncogene* **38**, 2800–2813 (2019).

1335   58.   Doench, J. G. *et al.* Optimized sgRNA design to maximize activity and minimize off-target

1336   effects of CRISPR-Cas9. *Nat. Biotechnol.* **34**, 184–191 (2016).

1337   59.   JG, D. Am I ready for CRISPR? A user's guide to genetic screens. *Nat. Rev. Genet.* **19**,

1338   (2018).

1339   60.   Li, W. *et al.* MAGeCK enables robust identification of essential genes from genome-scale

1340   CRISPR/Cas9 knockout screens. *Genome Biol.* **15**, 554 (2014).

1341   61.   Drygin, D. *et al.* Targeting RNA polymerase I with an oral small molecule CX-5461

1342   inhibits ribosomal RNA synthesis and solid tumor growth. *Cancer Res.* **71**, 1418–30

1343   (2011).

1344   62.   Haddach, M. *et al.* Discovery of CX-5461, the first direct and selective inhibitor of RNA

1345   polymerase I, for cancer therapeutics. *ACS Med. Chem. Lett.* (2012).

1346   doi:10.1021/ml300110s

1347   63.   Li, L. *et al.* CX-5461 induces autophagy and inhibits tumor growth via mammalian target

1348   of rapamycin-related signaling pathways in osteosarcoma. *Onco. Targets. Ther.* **9**, 5985–

1349   5997 (2016).

1350   64.   Maclachlan, K. H. *et al.* Novel Combination Therapies with the RNA Polymerase I

1351   Inhibitor CX-5461 Significantly Improve Efficacy in Multiple Myeloma. *Blood* **130**, 1805–

1352   1805 (2017).

1353   65.   Ritz, C., Baty, F., Streibig, J. C. & Gerhard, D. Dose-Response Analysis Using R. *PLoS*

1354   *One* **10**, e0146021 (2015).

1355   66.   A, I., L, H., T, A. & J, T. SynergyFinder: a web application for analyzing drug combination

1356   dose-response matrix data. *Bioinformatics* **33**, (2017).

1357   67.   Pugh, T. J. *et al.* The genetic landscape of high-risk neuroblastoma. *Nat. Genet.* **45**, 279–

1358   84 (2013).

1359   68.   McLeod, C. *et al.* St. Jude Cloud—a Pediatric Cancer Genomic Data Sharing Ecosystem.

1360   *bioRxiv* 2020.08.24.264614 (2020). doi:10.1101/2020.08.24.264614

1361